2020

Multi-objective Optimization of Multi-loop Control Systems

Yuekun Chen
1102306990@qq.com

MULTI-OBJECTIVE OPTIMIZATION OF MULTI-LOOP CONTROL SYSTEMS

A thesis submitted to
the Graduate College of
Marshall University
In partial fulfillment of
the requirements for the degree of
Master of Science
In
Mechanical Engineering
by
Yuekun Chen
Approved by
Dr. Yousef Sardahi, Committee Chairperson
Dr. Gang Chen
Dr. Mehdi Esmaeilpour

Marshall University
May 2020

APPROVAL OF THESIS

We, the faculty supervising the work of Yuekun Chen, affirm that the thesis titled *"Multi-Objective Optimization of Multi-loop Control Systems"*, meets the high academic standards for original scholarship and creative work established by the Master of Science in Mechanical Engineering and the College of Information Technology and Engineering. This work also conforms to the editorial standards of our discipline and the Graduate College of Marshall University. With our signatures, we approve the manuscript for publication.

Dr. Yousef Sardahi	Committee Chairperson	Date 03/03/2020
Dr. Gang Chen,	Committee Member	Date 3/4/2020
Dr. Mehdi Esmaeilpour	Committee Member	Date 03/04/2020

ACKNOWLEDGMENTS

I would like to express my gratitude to all those who helped me during the writing of this thesis. I gratefully acknowledge the help of my supervisor, Dr. Yousef Sardahi, who has offered me valuable suggestions in the academic studies. Without his consistent and illuminating instruction, this thesis could not have reached its present form.

Second, I would like to express my heartfelt gratitude to my thesis committee: Dr. Gang Chen and Dr. Mehdi Esmaeilpour, for their instruction and assistance.

Finally, I would like to thank my beloved family and my friends for their continuous support and encouragement. Without their trust and help, I couldn't have the strong motivations to urge me working hard on this thesis. Thank you all.

TABLE OF CONTENTS

LIST OF TABLES

LIST OF FIGURES

ABSTRACT

Cascade Control systems are composed of inner and outer control loops. Compared to the traditional single feedback controls, the structure of cascade controls is more complex. As a result, the implementation of these control methods is costly because extra sensors are needed to measure the inner process states. On the other side, cascade control algorithms can significantly improve the controlled system performance if they are designed properly. For instance, cascade control strategies can act faster than single feedback methods to prevent undesired disturbances, which can drive the controlled system's output away from its target value, from spreading through the process. As a result, cascade control techniques have received much attention recently. In this thesis, we present a multi-objective optimal design of linear cascade control systems using a multi-objective algorithm called the non-dominated sorting genetic algorithm (NSGA-II), which is one of the widely used algorithms in solving multi-objective optimization problems (MOPs). Two case studies have been considered. In the first case, a multi-objective optimal design of a cascade control system for an underactuated mechanical system consisting of a rotary servo motor, and a ball and beam is introduced. The setup parameters of the inner and outer control loops are tuned by the NSGA-II to achieve four objectives: 1) the closed-loop system should be robust against inevitable internal and outer disturbances, 2) the controlled system is insensitive to inescapable measurement noise affecting the feedback sensors, 3) the control signal driving the mechanical system is optimum, and 4) the dynamics of the inner closed-loop system has to be faster than that of the outer feedback system. By using the NSGA-II algorithm, four design parameters and four conflicting objective functions are obtained. The second case study investigates a multi-objective optimal design of an aeroelastic cascade controller applied to an aircraft wing with a leading and trailing control surface. The dynamics of

the actuators driving the control surfaces are considered in the design. Similarly, the NSGA-II is used to optimally adjust the parameters of the control algorithm. Ten design parameters and three conflicting objectives are considered in the design: the controlled system's tracking error to an external gust load should be minimal, the actuators should be driven by minimum energy, and the dynamics of the closed-loop comprising the actuators and inner control algorithm should be faster than that of the aeroelastic structure and the outer control loop. Computer simulations show that the presented case studies may become the basis for multi-objective optimal design of multi-loop control systems.

CHAPTER 1: INTRODUCTION

1.1 Literature Review

Cascade control techniques can improve significantly the performance of feedback controllers. Unlike single feedback control loops, cascade control strategies can act quickly to prevent external excitations from propagating through the process and making the controlled variable deviate from its desired level (Smith & Corripio, 1985). This important benefit has made these control methods very attractive to many applications such as chemical process industries and mechanical systems. However, the performance of the cascade control systems largely relies on tuning of the setup parameters of both inner and outer loops (Lee et al., 1998). Moreover, the tuning process should often satisfy multiple and conflicting objectives. One of the main objectives in designing cascade controllers is to make the inner loop fast and responsive in order to minimize the effect of upsets on the primary controlled variable (Smith & Corripio, 1985). Other objectives such as robustness against unavoidable measurements' noise and energy saving are also of high importance.

Cascade controllers have been in focus for a long time. They were first introduced by Franks and Worley in 1956 (Franks & Worley, 1956). After that, they have gained significant attention from control system researchers. For instance, Maffezzoni and his co-authors (Maffezzoni et al., 1990) proposed a new design concept for cascade control that aimed to attain four goals: 1) decoupling the design of inner from the outer control loop, (2) the outer loop stability should not be affected by the possible parameter variations in the inner loop, (3) elimination of the windup problems in the cascade structure; and (4) robustness of the overall closed-loop system. The proposed method was applied to steam temperature control application and it was shown that it can be used to handle any number of nested cascaded control loops. PID

(Proportional-Integral-Derivative)-based inner and outer control loops were designed and tuned by Maclaurin series and compared with those obtained by frequency and ITAE (integral-time-absolute error) methods (Lee et al., 1998). Also, a two-degree-of-freedom PID controller was designed to ensure the stability of cascade control (Alfaro et al., 2008). The outer loop gains were designed to automatically adjust their values when the inner loop controller changes. Another application can be found by Kaya et al. (2007). In the outer loop, a PI-PD Smith predictor scheme was used, while an internal model control was chosen for the inner loop of the cascade control. The outer and inner control parameters were obtained by minimizing one of the standard forms (different versions of the closed-loop system tracking error). Both first-order and second-order plants with time delay were used in the computer simulations. The results showed that the proposed technique is superior to single feedback methods. A PI controller for flux regulation was designed first to achieve fast direct flux control. After that, cascade schemes of PI torque and speed controllers were introduced to achieve high performance speed control of a permanent magnet synchronous motor (Chen et al., 2009). The performance of the proposed control scheme was tested in the presence of both load disturbance and parameter variations. A Hybrid PID cascade control was investigated (Homod et al., 2010) and implemented on HVAC (Heating, Ventilation, and Air Conditioning) systems in order to enhance the performance of the central air-conditioning system. The cascade control was tested and compared with the traditional PID that was tuned by Ziegler-Nichols tuning method. Using a mathematical model of the air-conditioning space, the simulations showed that the proposed hybrid PID-cascade controller has the capability of self-adapting to system variations and results in quicker response and better performance. A high-order differential feedback cascade controller was implemented instead of the conventional PID cascade control to regulate steam temperature of a power plant

boiler (Wei et al., 2010). The findings showed that the proposed control method has good static and dynamic performance, robustness, and disturbance rejection ability. A cascade structure that implements a PI (proportional-integral) controller for the speed regulation in the outer loop and a P (proportional) controller for controlling a DC motor armature current in the inner loop was investigated by Bhavina et al. (2013). Both simulation and experimental results demonstrated that the cascade PID control performs better than single PID control. Likewise, Abdalla and his colleagues proposed a cascade control system for current and speed control of a DC motor (Abdalla et al., 2016). Two PI controllers were implemented in the primary and secondary control algorithm.

Nonlinear cascade controllers have been also found in the literature. For instance, an inner static and dynamic sliding-mode controls were designed by (Almutairi & Zribi, 2010) and then tested on a ball-beam system using both simplified and complete mathematical models of the system. Therein, the authors indicated that an outer controller can be implemented to further improve the stability of the system, whilst by Chen et al. (2010), a hybrid nonlinear and linear cascade control was designed and analyzed for a boost converter. The inner current loop is a sliding-mode control and the outer voltage loop employs a PI control. Computer simulations showed that the reference output voltage can be tracked well with fast response even in the presence of parametric changes, system uncertainties, or external disturbances. While by Tunyasrirut and Wangnipparnto (2007), a Fuzzy–PID cascade controller to control the level of horizontal tank was developed. The cascade control structure was made of a PID controller in the inner loop for regulating the flow rate of the system and a Fuzzy logic controller in the outer loop for controlling the liquid level. The results showed that the effect of load disturbance is minimal, and the controlled system response does not overshoot when the cascade controller is applied.

Another nonlinear cascade loop based on type 2 fuzzy PD controller was used by Hamza et al. (2015) to balance the pendulum of a rotary inverted pendulum system about its upright unstable equilibrium position. The parameters of the master and slave controllers were optimized by using genetic algorithm and particle swarm optimization. A single cost function that consists of the steady state error, settling time, rise time, maximum overshoot, and control energy was formulated. Experimental and simulation results manifested that the proposed control system is robust against load disturbances, parameter variations, and measurement noises.

Multi-objective optimization of cascade controllers has been rarely discussed in the literature. Only a few studies can be found in this regard. For instance, Kumar and his colleagues (Kumar et al., 2012a) developed a multi-objective optimal control of a multi-loop controller consiting of a PI controller in its inner and outer loop. The control algorithm was used to regulate the liquid level in a cylindrical tank. Two algorithms, NSGA - II and NSPSO (Non-dominated Sorting Particle Swarm Optimization), were used to tune the control gains via minimizing tracking error and maximizing disturbance rejection. The solution of the MOP in terms of the Pareto set and Pareto front were obtained. The results showed the competing nature between the selected design objectives. Similarly, an optimal cascade controller comprising two PI controllers, one used in the primary and the other in the secondary loop, were presented by Agees Kumar and Kesavan Nair (2012) to control the level in a cylindrical tank. Both NSGA - II and NSPSO were utilized to fine tune the controller parameters of both control loops and achieve two objectives: minimum overshoot and settling time. Another study that concerns the optimization of cascade controllers was introduced by Fu et al. (2017). Therein, the cascade controller was used to improve the performance of a superheated steam temperature system and the optimization process was broken in two stages. In the first stage, the gains of a PI controller

in the inner loop were optimized by considering the tracking error and disturbance rejection as fitness functions. Also, the robustness of the closed-loop system in terms of the sensitivity function was imposed as a constraint during the optimization process. In the second stage, the outer PI controller was fine-tuned by maximizing the robustness and disturbance rejection of the controlled system at the same time. The computer simulations showed a promising future of the proposed controller in industrial applications.

Although a couple of studies have addressed the design of cascade controllers in multi-objective scope, the main purposes of these controllers have not been considered. There are two main goals that have to be achieved in the design of cascade controllers: 1) the salve closed-loop control system must be faster than the master, 2) the secondary loop should fast reject any disturbance and prevent it from propagating to the primary loop. Other objectives such as robustness against measurement noise, optimum energy consumption, small overshoot, fast transient response, and minimum tracking or steady-state error are legitimate and traditional requirements in control systems' design. Thus far, most of the studies have focused on the disturbance rejection capability of cascade algorithms and used that as one of the objectives during the optimization process, see for example the works by Kumar et al. (2012b) and Fu et al. (2017). The fact that the inner closed-loop system has to be faster than the outer closed-loop one has been ignoned during the optimization and the authors sufficed to show that it is satisfied only on the simulation or exprimental results; that is, it was not considered as one of the design objectives. On the other hand, some studies considerd completely different objctives in the design of cascade control systems. For example, Kumar and Nair (2012) designed an optimal multi-loop system by optimizing the overshoot and settling time of the closed-loop system. Although these are important objectives, the two main goals the cascade loops were introduced

for should be also included. On the other side, attaining the prime properties of cascade schemes come at the cost of control energy consumption; particularly, a large control signal is required for better disturbance rejection. In other words, the objective of minimizing the control energy is conflicting with maximizing the ability of closed-loop system to reject external upsets. For this reason and since energy saving is important nowadays, the control energy should be considered as one of the cost functions in the design of nested loop controllers. However, this objective has been ignored by almost all the recent studies in this context. Furthermore, other design targets such as improving the insensitivity of the closed-loop cascade system to measurement noise is also important for two reasons: 1) most measurement devices are susceptible to noise, and 2) the goal of maximizing the measurement noise rejection is competing with that of maximizing the power of the controlled system to repudiate external disturbances.

In the forthcoming sections, we introduce the concept of multi-objective optimization, delineate the working principle of NSGA-II, elaborate on the structure of cascade control systems, and outline the thesis.

1.2 Multi-Objective Optimization

Multi-objective optimization problems (MOPs) have received much attention recently because of their enormous applications. A MOP can be stated as follows:

$$\min_{k\in D}\{\mathbf{F}(\mathbf{k})\}, \tag{1}$$

where **F** is the map that consists of the objective functions f_i: D $\rightarrow R^1$ under consideration.

$$\mathbf{F}\text{: D}\rightarrow \mathbf{R}^{\text{k}},\ \mathbf{F}(\mathbf{k}) = [f_1(\boldsymbol{k}),\ \dots,\ f_k(\boldsymbol{k})]. \tag{2}$$

$\mathbf{k}\in\ \boldsymbol{D}$ is a d-dimensional vector of design parameters. The domain D$\subset \mathbf{R}^{\boldsymbol{d}}$ can in general be expressed by inequality and equality constraints:

$$D = \{\mathbf{k}\ \in \mathbf{R}^d |\ g_i(\mathbf{k}) \le 0, i = 1, \dots, l, and\ \ h_j(\mathbf{k}) = 0, j = 1, \dots, m\ \}. \tag{3}$$

Where there are *l* inequality and *m* equality constraints. The solution of MOPs forms a set known as the Pareto set and the corresponding set of the objective values is called the Pareto front. The dominancy concept (Marler & Arora, 2004) is used to find the optimal solution. The MOPs are solved using multi-objective optimization algorithms. These methods can be classified into scalarization, Pareto, and non-scalarization non-Pareto methods (Sardahi, 2016).

The scalarization methods such as the weighted sum, goal attainment, and lexicographic approach require transformation of the MOP into a single optimization problem (SOP) (Pareto, 1971), normally by using coefficients, exponents, constraint limits, etc.; and then methods for single objective optimization are utilized to search for a single solution. Computationally, these methods find a unique solution efficiently and converge quickly. However, these methods cannot discover the global Pareto solution for non-convex problems. Also, it is not always obvious for the designer to know how to choose the weighting factors for the scalarization (Hernández, et al., 2013).

Unlike the scalarization methods, the Pareto methods do not aggregate the elements of the objectives into a single fitness function. They keep the objectives separate all the time during the optimization process. Therefore, they can handle all conflicting design criteria independently, and compromise them simultaneously. The Pareto methods provide the decision-maker with a set of solutions such that every solution in the set expresses a different trade-off among the functions in the objective space. Then, the decision-maker can select any point from this set. Compared to the scalarization approaches, the Pareto methods can successfully find the optimal or near optimal solution set, but they are computationally more expensive. Examples of algorithms that fall under this category are the MOGA (Multiple Objective Genetic Algorithm), PSO (Particle Swarm Optimization), NSGA-II (Non-dominated Sorting Genetic Algorithm), SPEA2 (Strength

Pareto Evolutionary Algorithm), and NPGA-II (Niched Pareto Genetic Algorithm). Mainstream evolutionary algorithms for MOPs include NSGA-II, multi-objective particle swarm optimization (MOPSO) and strength Pareto evolutionary algorithm (SPEA). Deterministic methods such as set oriented methods with subdivision techniques, and multi-objective algorithms based on the simple cell mapping (SCM) can be also used to find the solution set (Sardahi, 2016).

The $\epsilon-$constraint method and the VEGA (Vector Evaluated Genetic Algorithm) approach are examples of the non-scalarization non-Pareto methods. In the $\epsilon-$constraint method, one of the cost functions is selected to be optimized and the rest of the functions in the objective space are converted into constraints by setting an upper bound to each of them. The VEGA works almost in the same way as the single objective genetic algorithm, but with a modified selection process. A comprehensive survey of the methods used for solving MOPs can be found in the work of Jones et al. (2002), Marler and Arora (2004), and Tian et al. (2017).

Cascade control systems can be optimally designed by using any one of these techniques. Control systems' design problems are complex and nonconvex, therefore evolutionary algorithms are the methods of choice (Woźniak, 2010). They outperform classical direct and gradient based methods which suffer from the following problems when dealing with non-linear, non-convex, and complex problems: 1) the convergence to an optimal solution depends on the initial solution supplied by the user, and 2) most algorithms tend to get stuck at a local or sub-optimal solution. On the other side, evolutionary algorithms are computationally expensive (Hu et al., 2003). However, this cost can be justified if a more accurate solution is desired and the optimization is conducted offline. The most widely used multi-objective optimization algorithm is the NSGA-II (Sardahi & Boker, 2018; Xu et al., 2018). It yields a better Pareto front as

compared to SPEA2 and PESA-II (Pareto Envelope based Selection Algorithm) (Gadhvi et al., 2016). Therefore, in this thesis, we use the NSGA-II to solve the multi-objective control problem.

1.3 NSGA-II

NSGA (Srinivas & Deb, 1994) is a non-domination based genetic algorithm. Even though it performs well in solving MOPs, its high computational effort, lack of elitism, and the implementation of what is called sharing parameter had necessitated improvements. As a result, a modified version of the algorithm named NSGA-II was presented by Deb et al. (2002). The new version has a better sorting algorithm, includes elitism, eliminates the need for the sharing parameter, and has less computational burden. As shown in Figure 1, the algorithm incorporates eight basic operations: Initialization, fitness evaluation, non-domination ranking, crowding distance calculation, tournament selection, crossover, mutation, and combination (Deb et al., 2002).

The algorithm starts with the initialization process in which a random population, *Npop*, that satisfies the lower and upper bound constraints is generated. Once the population is initialized, fitness function evaluations, *F(Pop)*, takes place in the second stage. Using these function values, the candidate solutions are sorted based on their non-domination and placed into different fronts. The solutions in the first front dominate all the other individuals while those in the second front are dominated only by the members in the first front. Similarly, the solutions in the third front are dominated by individuals in both the first and second fronts, and so on. Each candidate solution is given a rank number, *rnk*, of the front where it resides. For instance, members in first front are ranked 1 and those in second are given a rank of 2 and so on.

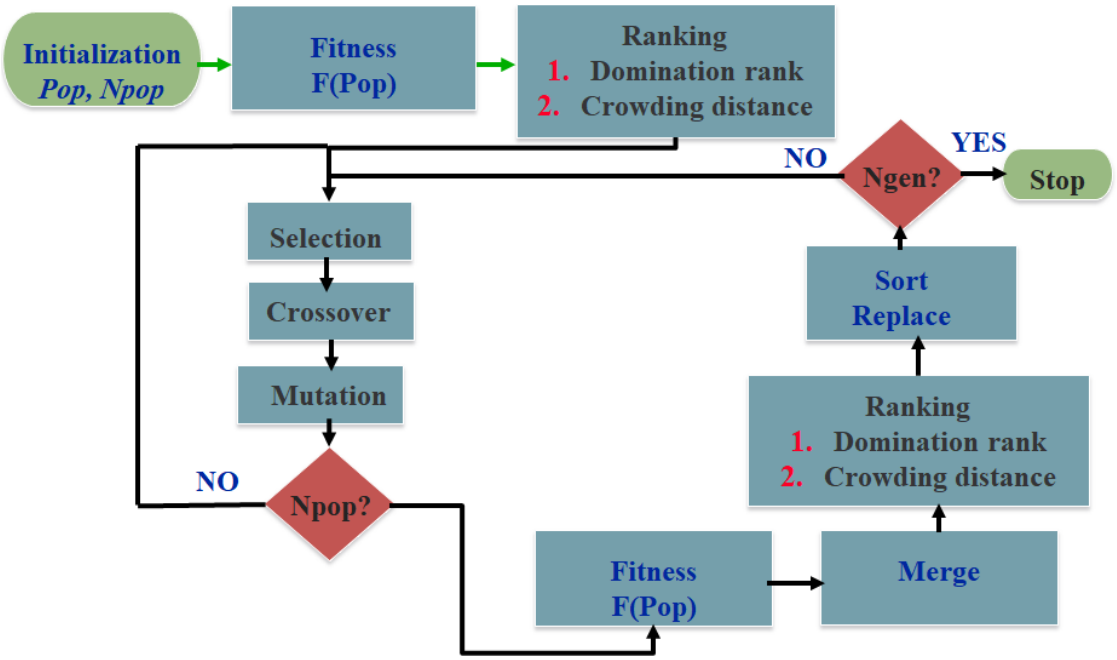

Figure 1: NSGA-II algorithm flowchart

To improve the diversity of the solution, a parameter called the crowding distance is computed for each solution. This parameter measures how close an individual is to its neighbors. The crowding distance is calculated front wise since comparing the crowding distance between two individuals from two different fronts is meaningless. The larger the average crowding distance, the better the diversity of the population. After that, the parents for the next generation are selected. One of the popular algorithms used for this purpose is the binary tournament selection method. At each iteration $i = 1 : n_c$, where $n_c = round(Npop = 2)$ and n_c is the number of parents, two random integer numbers are uniformly generated between 1 and $Npop$. These values are used to fetch two candidate parents from Pop. A candidate solution is selected if its rank is smaller than the other or if its diversity measure is bigger than the other. Then, a crossover algorithm such as the arithmetic crossover method (Beyer & Deb, 2001; Deb & Agrawal, 1995) and a mutation algorithm such as the simple mutation approach (Kakde, 2004)

are applied on the selected parents to produce new children. These two operations are repeated n_c times which result in a new offspring of size $Npop$. Elaborated details about crossover and mutation methods can be found in the work of Haupt and Haupt (2004). After that, the new children are merged with the current population. This combination guarantees the elitism of the best individuals. Finally, individuals are sorted based on their crowding distance and rank values. First, the sorting is performed with respect to the crowding distance in a descending order. Then, an ascending order of the population is followed based on the rank values. The new generation is produced from the sorted population until the size reaches $Npop$. If the number of generations, *gen*, is not equal to the maximum number of iterations, *Ngens*, the selection, crossover, mutation, merging, ranking and sorting process are repeated.

NSAG-II works well on two-objective and three-objective problems. For many-objective optimization problems (with more than three objectives), large populations are used to enhance the searchability of the algorithm but at the expense of the computation time (Shibuchi et al., 2009). A study on the effect of size of the decision variable space on the performance of NSGA-II and other evolutionary algorithms showed that NSGA-II converges to the true Pareto front on all the test problems when the number of design parameters is less than or equal to 128 (Durillo et al., 2008; Durillo et al., 2010). In this thesis, the size of the objective space is four at maximum and that of decision variable space is between four and ten. Therefore, NSGA-II is expected to perform well in solving the problems at hand.

1.4 Outline of the Thesis

This thesis is based on the author's research publications on multi-objective optimal design of multi-loop control systems in the past year. Chapter 2 proposes multi-objective optimal design of a cascade control system for a class of underactuated mechanical systems. Chapter 3 discusses

the multi-objective optimal design of an active and aeroelastic cascade control system applied to an aircraft's wing having a leading and trailing control surface. Chapter 4 summarizes the thesis and suggests the future directions.

CHAPTER 2: MULTI-OBJECTIVE OPTIMAL DESIGN OF A CASCADE CONTROL SYSTEM FOR A CLASS OF UNDERACTUATED MECHANICAL SYSTEMS

2.1 Cascade control systems

Consider the general representation of a two-level cascade control system shown in Figure 2. The plant under control is comprised of two subsystems with transfer functions $G_1(s)$ and $G_2(s)$. An inner $C_I(s)$ and outer $C_O(s)$ control loops are used to drive the systems to their desired states. Here $X_d(s)$ and $X_o(s)$ are the desired and the actual output of the outer subsystem, respectively, while, $X_{Id}(s)$, computed by the outer control algorithm to attain $X_d(s)$, and $X_I(s)$ are respectively the desired and the actual output of the inner subsystem. The inner and outer load disturbances are denoted by $D_I(s)$ and $D_O(s)$, respectively. The measurement noises affecting the inner and outer feedback sensors are denoted by $N_I(s)$ and $N_O(s)$, respectively. The control system design aims to alleviate the impacts of these unwanted signals, minimize the tracking error for both control loops, make the speed of response of the inner closed-loop system faster than that of the outer one, and reduce the amount of consumed control energy. To this end, these objectives should be quantitatively described.

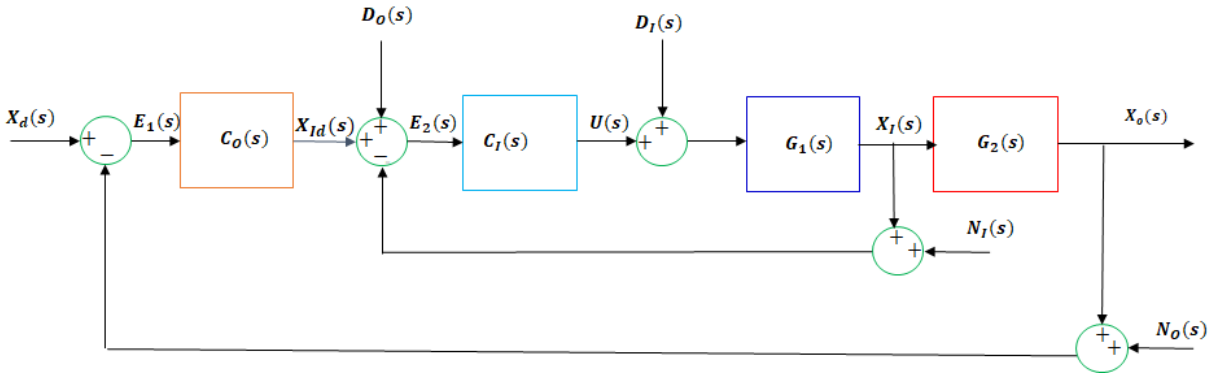

Figure 2: Block diagram of two-level cascade control system

When deriving the design objectives, we will assume that the inner and outer closed-loop subsystems control the desired signals perfectly. This simplifies the control design and the mathematical expressions of the fitness functions that will be used later in the multi-objective optimization. Using this assumption, understanding that the design is carried out in the frequency domain, and dropping *s* from the inputs and outputs, the relationship between the controlled variable, X_I and the load disturbance is denoted D_I; the tracking error of the inner closed-loop system E_2 and X_{Id} ; and X_I and inner stochastic noise N_I read

$$X_I \,/\, D_I = G_1 \,/(1 + C_I G_1), \tag{4}$$

$$E_2 \,/\, X_{Id} \; = 1/(1 + C_I G_1), \tag{5}$$

$$X_I \,/\, N_I = (-C_I G_1) \,/\, (1 + C_I G_1), \tag{6}$$

from these equations, we notice that for better tracking, and disturbance and noise attenuation, the ∞−norm of the following objectives should be minimized

$$f_1 = \sup_{\omega_1<\omega<\omega_2} \sigma(\|E_2 \,/\, X_{Id}\,\|_\infty), \tag{7}$$

$$f_2 = \sup_{\omega_3<\omega<\omega_4} \sigma(\|X_I \,/\, N_I\|_\infty). \tag{8}$$

where σ is the largest singular value among the transfer functions. The symbol *sup* indicates the largest gain among the gain vector elements is minimized to account for the worst-case scenario. The variables ω_1 , ω_2, ω_3, and ω_4 define the frequency ranges at which the noise and disturbance occur.

Assuming the dynamics of the inner loop which includes $C_I(s)$ and $G_I(s)$ is negligible (inner control loop is perfect), similar relationships between X_O and D_O; the tracking error of the outer closed-loop system E_1 and X_d; and X_o and inner stochastic noise N_o can be found as follows

$$X_o \,/\, D_O = G_2 \,/\, (1 + C_o G_2), \tag{9}$$

$$E_1 \,/\, X_d = 1/\,(1 + C_o G_2), \tag{10}$$

$$X_o \,/\, N_o = (-C_o G_2) \,/\, (1 + C_o G_2), \tag{11}$$

Similarly, we note that for better outer loop tracking, and disturbance and noise attenuation, the norm of the following functions should be minimized

$$f_3 = \sup_{\omega_1<\omega<\omega_2} \sigma(\|E_1 \,/\, X_d\|_\infty), \tag{12}$$

$$f_4 = \sup_{\omega_3<\omega<\omega_4} \sigma(\|X_o \,/\, N_o\|_\infty). \tag{13}$$

To ensure that the dynamics of the inner loop is faster than that of the outer loop, the closed-loop poles of the inner closed loop system must be placed on the *s*-plane to the left of those of outer closed subsystem. This can be achieved by defining two variables λ_I and λ_o as follows:

$$\lambda_I = max(real(eig(1 + C_I G_1))), \tag{14}$$

$$\lambda_o = max(real(eig(1 + C_o G_2))), \tag{15}$$

Here, *eig* denotes the mathematical operation that result in the eigenvalues of the corresponding equation, *real* extracts the real part from the poles, and *max* returns the maximum pole. That is, these two equations will return the locations of the inner and outer closed-loop dominate poles, which dictate the system response. Therefore, λ_I has to be less than λ_o or the ratio λ_o/λ_I must be less than 1 to guarantee that the inner closed-loop reacts faster than the outer one.

To save the amount of control energy, we minimize the Frobenius norm, $\|.\|_F$, of the outer and inner control gains

$$f_5 = \|\mathbf{k}\|_F, \tag{16}$$

where, **k** is a vector containing the setup parameters of the control algorithms.

2.2 Underactuated Ball and Beam System

Consider the ball and beam system shown in Figure 3. The system is comprised of two plants: the rotary servo motor and the ball and beam. The DC (Direct-Current) servo motor described by the following transfer function

$$G_1(s) = \frac{\Theta_l(s)}{U(s)} = \frac{K}{s(\tau s+1)}, \quad (17)$$

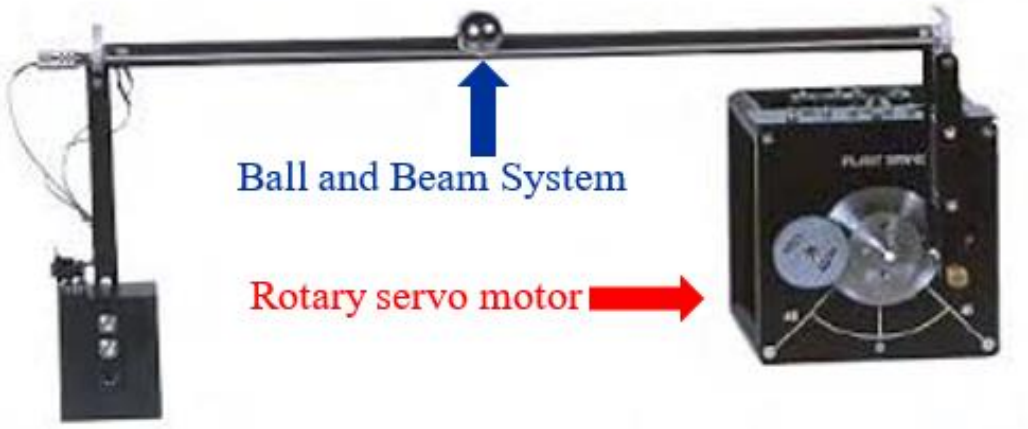

Figure 3: Ball and beam system

Where $\Theta_l(s)$ is the Laplace transform of the load shaft position $\theta(t)$, $U(s)$ is the Laplace transform of the motor input voltage $u(t)$, K = 1.53 *rad*/ (V.s) is the steady-state gain, and τ = 0.0253 s is the time constant. A linearized model that describes the position of the ball, $X(s)$, relative to the angle of the servo load gear reads:

$$G_2(s) = \frac{\mathrm{X}(s)}{\Theta_l(s)} = \frac{K_b}{s^2}. \quad (18)$$

Here, K_b = 0.419 $m/(rad.s^2)$.

Now consider the general cascade control shown in Figure 2 with $G_1(s)$ and $G_2(s)$ represent the dynamics of the DC motor and the ball-beam system, respectively. The output of the outer system, X_o, is the actual position of the ball and the output of the inner one, X_I, is the

actual position of the load shaft, $\Theta_l(s)$. The desired position of the ball is denoted by X_d and desired shaft angle is represented by X_{Id}. N_O(s) is a random noise affecting the reading of the sensor that measures the ball position, while N_I(s) is the measurement noise in the DC motor angle estimation. An external excitation that alters the position of the motor's shaft is denoted by D_I(s) while the affects of the position of the ball on the beam is denoted by D_O(s). The inner loop implements an ideal PD (Proportional-derivative) controller to manage the position of the servo motor shaft. The controller dynamics can be described by the following transfer function

$$C_I(S) = \frac{U(s)}{E_2(s)} = K_{pi} + K_{di}s, \tag{19}$$

where, K_{pi} and K_{di} are the proportional and the derivative gains, respectively. The characteristic equation of the inner loop system, A_I(s), is given by

$$A_I(\mathrm{s}) = s^2 + \frac{1+KK_{di}}{\tau}s + \frac{KK_{pi}}{\tau}, \tag{20}$$

the dominant pole of the inner closed-loop system can be found from

$$\lambda_I = max(real(eig(A_I(\mathrm{s}) = 0\ ))), \tag{21}$$

Stability analysis suggests that K_{pi}> 0 and K_{di}>*−1/K* for the closed-loop system to be stable. We assume that the inner loop controller can perfectly track the desired shaft angle. With that in mind, we choose a dynamic PD controller for the outer loop

$$C_O(S) = \frac{X_{Id}(s)}{E_1(s)} = K_{do}(K_{po} + s), \tag{22}$$

here, K_{po} and K_{do} are the setup parameters of the control system. As stated above, if we assume that the inner loop can manage the dynamics of the servo motor and move the shaft to the desired position, $X_{Id}(s)$, that will bring the ball to its desired location $X_d(s)$. Using this assumption, we set the closed-loop transfer function of the inner system (servo motor under PD controller) to unity. Then, the closed-loop characteristic equation of the outer loop system, A_o(s), is given by

$A_o(\mathrm{s}) = s^2 + K_b K_{do} s + K_b K_{do} K_{po}.$ (23)

as a result, the pole that dominates the dynamics of the outer control loop is given by

$\lambda_o = max(real(eig(A_o(\mathrm{s}) = 0\ )))$. (24)

For the outer loop to be stable, K_{po} and K_{do} must be greater than zero. These tunable gains in addition to those of the inner controller will be tuned and the optima trade-offs among the design requirements will be found.

2.3 Multi-Objective Optimal Design

In the multi-objective optimal design, we take the elements of the inner and outer control algorithms as the design parameters. That is **k** of Eq. (1) and Eq. (16) is given by **k** = $[K_{pi}, K_{di}, K_{po}, K_{do}]$. The design space for the parameters is chosen as follows,

$Q = \{k \in [0.1,50] \times [-0.6,1] \times [0,5] \times [0.1,19] \sqsubset \mathbf{R}^4\}$. (25)

We notice that these ranges satisfy the stability requirements stated in Eqs. (20) and (23). The MOP is stated as

$\min_{K \in Q} \{F_1, F_2, \|\mathbf{k}\|_F, r\}$, (26)

Where, $F_1 = (f_1 + f_3)/2$ is the objective that aims to enhance the tracking error and disturbance attenuation of the inner and outer closed-loop subsystems as shown in Eqs. (7) and (12). The function $F_2 = (f_2 + f_4)/2$ combines the fitness functions in Eqs. (8) and (13) and represents the $\infty-$norm of the transfer functions relating the output of either the inner or outer control system to the measurement noise. Measurement noises are typically dominated by high frequencies while load disturbances are dominated by low frequencies (Sardahi & Boker, 2018). Therefore, in this paper, we assume the frequency of the noises is in the range $\omega \in [100,10^5]$ *rad/s*, while that of the disturbance belong to $\omega \in [0.0001,2]$ *rad/s*.

Minimizing these norms ensures that the tracking error is small; the closed-loop system is insensitive to unavoidable measurements' noise and disturbances; and the control energy is minimum. Furthermore, we need the response of the inner controlled system to be faster than the outer one. To this end, we minimize *r* given by the following equation

$$r = \lambda_o / \lambda_I \tag{27}$$

It is obvious that small values of *r* indicate that the inner closed-loop system is faster than the outer one. Making the inner loop faster than the outer one ensures operational safety in the face of internal and external perturbations (Habibi et al., 2008). To solve this multi-optimization problem, the nondominated sorting genetic algorithm (NSGA-II) is used. The reader can refer to Deb, K. (2001) for more details about this algorithm. According to the MATLAB documentation, the population size can be set in different ways and the default population size is 15 times the number of the design variables *nvars*. Also, the maximum number of generations should not exceed 200×*nvars*. In this study, the population size is set to 400, and the number of generations is set to 400.

2.4 Results and discussion

Different projections of the Pareto front and Pareto set, poles' map of the inner and outer closed-loop subsystems, and the controlled system response to disturbance and measurement noise at different objective values are discussed here. The optimization problem at hand is 4×4. That is, 4 design parameters and 4 objectives. The Pareto set which contains the optimal values of the decision variables is shown in Figure 4 and different projections of the corresponding Pareto fronts are plotted in Figures 5 and 6. The color in these figures is mapped to the value of $\|\mathbf{k}\|_F$ where red denotes the highest value, and dark blue denotes the lowest value. This coloring adds a 3D projection to these figures. It also shows the corresponding design variables from the

Pareto set for each point on the Pareto front. The Pareto set shows that large control energy consumption is associated with high K_{pi} and $K_{do} \times K_{po}$ values. The Figure 4(b) also shows that most of the optimal values of K_{po} and K_{do} are concentrated on the right side of the graph. However, the optimal values of K_{pi} and K_{di} spread between their specified stable ranges. This can be explained by examining Eqs. (19) and (22) where the proportional gain in the later equation is scaled by K_{do}. Empty regions indicate the non-existence of optimal solutions that satisfy the optimization constraints.

The Pareto front in Figure 5 demonstrates competing relationship between F_1 and $\|\mathbf{k}\|_F$, and between F_2 and $\|\mathbf{k}\|_F$, meaning, large control energy is needed to achieve small tracking errors and better disturbance rejections (see Figure 5(a)). On the other side, better attenuation of the measurement noise can be only achieved when the control energy is small (see Figure 5(b)). That is to say, the objective of minimizing the effect of measurement noise is also conflicting with that of reducing the impact of external disturbance as shown in Figure 6(a). The figure also shows that after F_1 = 0.3, F_2 goes up and then decreases as F_1 increases. This occurs because of the size of the objective space which includes 4 conflicting objectives. These conflicting relationships have been reported in many control books (Dorf & Bishop, 2011; Ogata & Yang, 2010; Franklin et al., 1994). This stresses the fact that the design of control systems should be conducted in multi-objective settings to account for all the trade-offs among the design targets. Another conflicting relationship between objectives can be found in Figure 6(b). It can be noticed that the goal of making the dynamics of the inner closed-loop system faster than that of the outer closed-loop system is in non-agreement with that of energy consumption. The pole maps of the inner and outer controlled systems are shown in Figure 7. As indicated by the color code and the scale of the *Re(s)-axis*, the poles of inner closed-loop system are located to the left

of those of the outer controlled system. In other words, the objective to make the dynamics of the outer loop dominates that of the inner closed-loop was successfully achieved by the MOP algorithm.

The responses of the inner and outer closed-loop systems at different values of *r* are shown in Figures 8 and 9 when $d_i(t) = d_o(t) = 0.5sin(t)$. Here, $d_i(t)$ and $d_o(t)$ are the inverse Laplace of $D_I(s)$ and $D_O(s)$ labeled in Figure 2. We assume that external disturbances on the inner and outer loop are low frequency signals with period $T = 2\pi$ seconds which agrees with frequency range selected in Chapter 2.3. In Figure 8, although the response of the inner closed-loop system is almost two times that of the outer system, the tracking error is bad since the inner loop is not fast enough to prevent the propagation of the disturbance to the outer loop. While in Figure 9, the dynamics of the inner subsystem is approximately 14 times faster than that of the outer subsystem and the result is better tracking error since the inner controlled system is fast enough to reduce the effect of the upsets on the system response. It is worth mentioning that the later response occurs at the expense of the controlled energy.

To get more insight into the ability of the system to reject unwanted signals, the time response of the controlled system $X_o(t)$, which denotes the inverse Laplace of $X_O(s)$ shown in Figure 2, is graphed at the minimum and maximum value of the first design objective, F_1. Here, the load disturbances are modeled by harmonic signal, $d_i(t) = d_o(t) = 0.5sin(t)$. As expected and evident from Figure 10, the best and worst disturbance rejection occur respectively at min (F_1) and max (F_1). It should be indicated here that high control energy is required to achieve small tracking error and better disturbance rejection. This can be readily observed from Figure 11 where the large values of $\|\mathbf{k}\|_F$ result in small steady-state errors and better repudiation of external disturbances. On other side, small values of $\|\mathbf{k}\|_F$ are appealing for better rejection of

measurement noise as shown in Figure 12. In Figure 12(a), F_2 = 0.0260 and $\|\mathbf{k}\|_F$ = 8.1890, while F_2 = 0.3129 and $\|\mathbf{k}\|_F$ = 52.5521 in Figure 12(b). The outer and inner measurement noise are assumed to be white noise *WN* signals with 0.1 variance and zero mean; that is $n_i(t) = n_o(t)$= *WN*. White noise covers wide spectrum of frequencies and is used frequently in testing controlled system behavior against sensor noises (Sardahi & Sun, 2017; Sardahi & Boker, 2018).

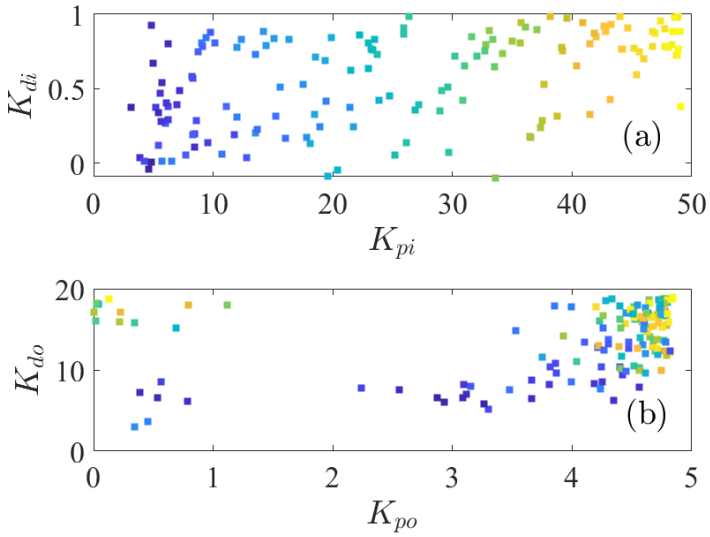

Figure 4: Projections of the Pareto set: (a) K_{di} versus K_{pi}, (b) K_{do} versus K_{po}. The color code indicates the level of $\|k\|_F$, where red denotes the highest value, and dark blue denotes the smallest.

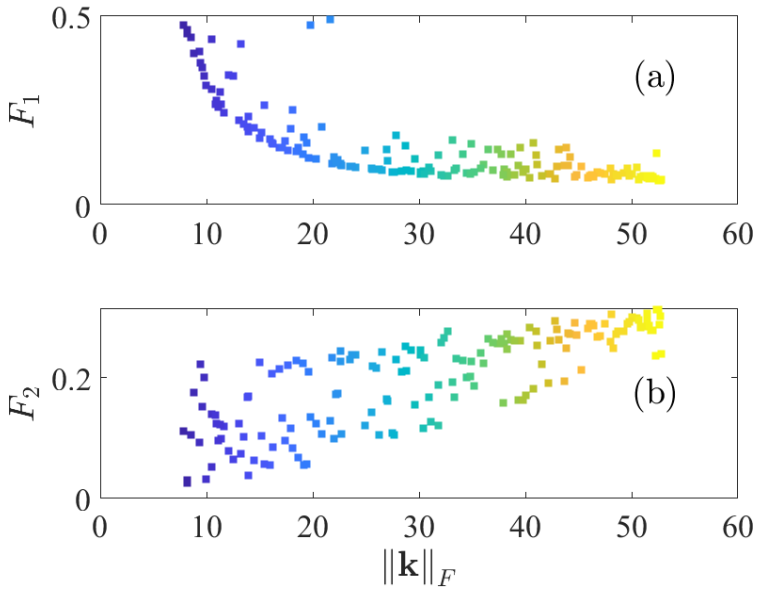

Figure 5: Projections of the Pareto front: (a) F_1 versus $\|k\|_F$, (b) F_2 versus$\|k\|_F$. The color code indicates the level of $\|k\|_F$, where red denotes the highest value, and dark blue denotes the smallest.

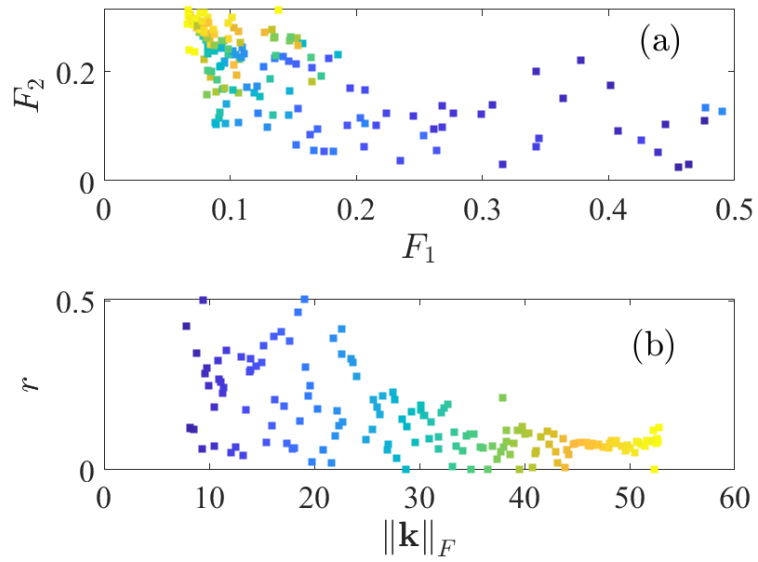

Figure 6: Projections of the Pareto front: (a) r versus$\|k\|_F$, (b) F_2 versus F_1. The color code indicates the level of $\|k\|_F$, where red denotes the highest value, and dark blue denotes the smallest.

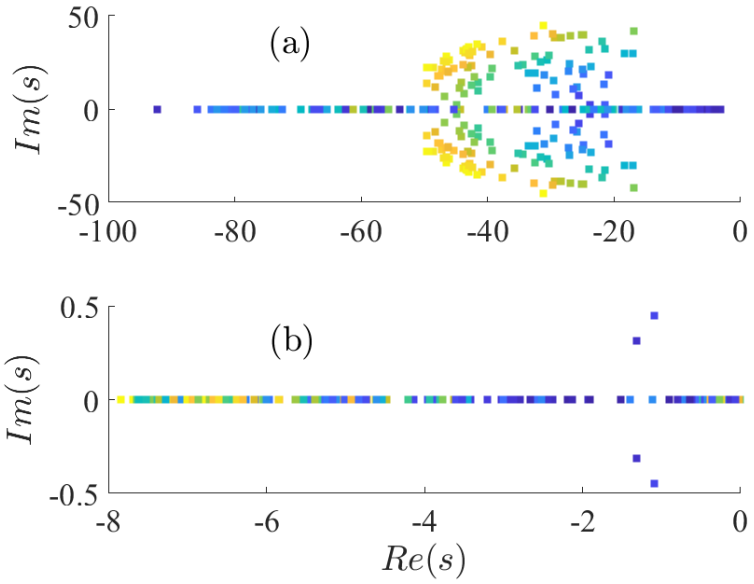

Figure 7: Pole maps, on the y-axis is the imaginary part of the pole, Im(s), and the x-axis is the real part of the pole, Re(s): (a) Pole map of the inner closed-loop system, (b) Pole map of the outer closed-loop system. The color code indicates the level of $\|k\|_F$, where red denotes the highest.

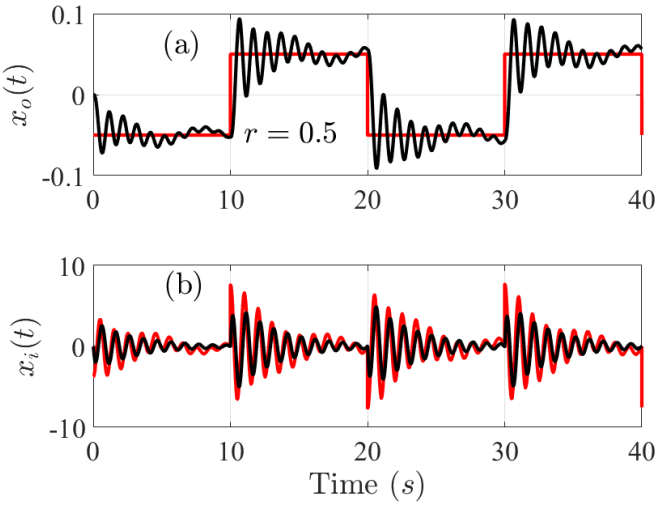

Figure 8: Outer and inner controlled systems' responses when r = 0.5 (a) Response of the outer closed-loop system $x_o(t)$versus time, (b) Response of the inner closed-loop system $x_o(t)$versus time. Red solid line: reference signal, Black solid line: actual system, response with d_i(t) = d_o(t) = 0.5sin(t).

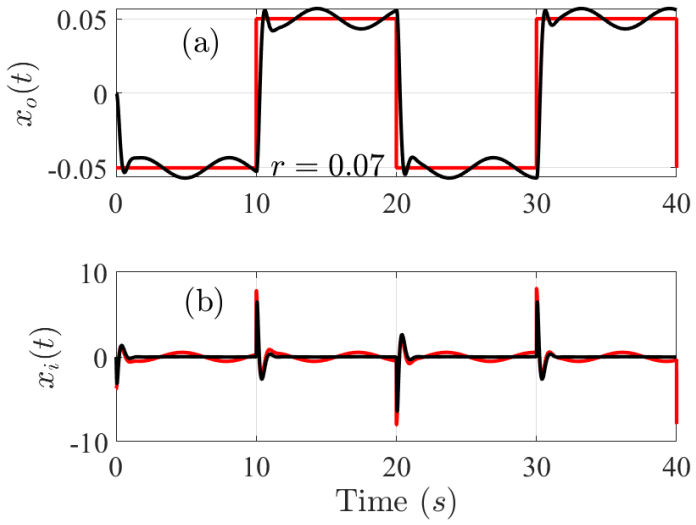

Figure 9: Outer and inner controlled systems' responses when r = 0.07 (a) Response of the outer closed-loop system $x_o(t)$versus time, (b) Response of the inner closed-loop system$x_o(t)$versus time. Red solid line: reference signal, Black solid line: actual system response with d_i(t) = d_o(t) = 0.5sin(t).

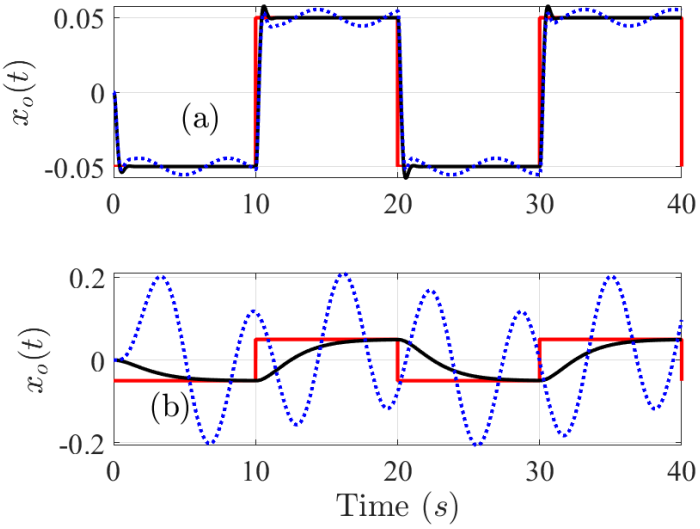

Figure 10: Ball position versus time. (a) Controlled system response at min (F_1), (b) Controlled system response at max (F_1). Red solid line: reference signal $x_d(t)$, black solid line: system response with d_i(t) = d_o(t) = 0, blue dotted line: system response with d_i(t) = d_o(t) = 0.5sin(t).

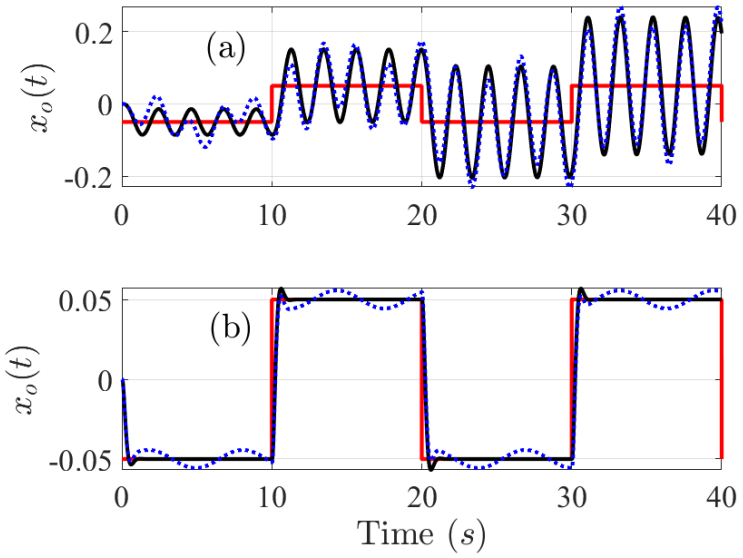

Figure 11: Ball position versus time. (a) Controlled system response at min ($\|k\|_F$), (b) controlled system response at max ($\|k\|_F$). Red solid line: reference signal $x_d(t)$, black solid line: system response with d_i(t) = d_o(t)= 0, blue dotted line: system response with d_i(t) = d_o(t)= 0.5sin(t).

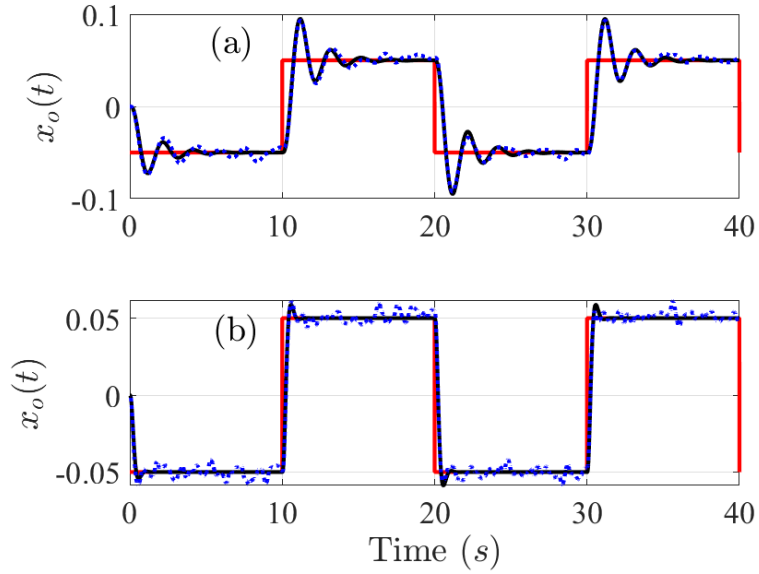

Figure 12: Ball position versus time. (a) Controlled system response at min (F_2), (b) Controlled system response at max (F_2). Red solid line: reference signal $x_d(t)$, black solid line: system response with n_i(t) = n_o(t) = 0, blue dotted line: system response with n_i(t) = n_o(t) = WN.

CHAPTER 3: MULTI-OBJECTIVE OPTIMAL DESIGN OF AN ACTIVE AEROELASTIC CASCADE CONTROL SYSTEM FOR AN AIRCRAFT WING WITH A LEADING AND TRAILING CONTROL SURFACE

3.1 Introduction

One of the important components of an aircraft is its flexible wing. Its design is very complex since it involves both structural, aerodynamic, and active control design. The active aeroelastic controls are necessary in order to achieve three goals: aircraft stability, flutter suppression, and gust load alleviation. Stability is the number one concern in the design of any control system, and control designers should make sure it is satisfied before they embark on improving the controlled system performance. Extending the airspeed flutter boundaries and ensuring the flexible structure is stable at higher airspeeds is also one of the important goals. Commonly, a 15% flutter-free margin is imposed above the design envelope in both civil and military aircrafts (Singh et al., 2016). Aerodynamic or gust loading is inevitable and reducing its effect is a must. Aeroelastic structures such as wings are driven by several control surfaces that have embedded actuators which are instructed by open loop or closed-loop control algorithms.

Active aerostatic controls of flexible structures such as aircrafts' wings have received much attention lately. State feedback controllers were discussed in a few works (Liebeck, 2004; Lucia, 2005; Gaspari et al., 2009; Zhao, 2009). Receptance-based active control systems for wings with single or multiple control surfaces were introduced in the works of (Singh et al., 2010; McDonough et al., 2011; Singh et al., 2014; Kumar et al., 2012b). In the design of the active control system, it is usually assumed that the actuator driving the control surface is perfect and can provide the desired control surface rotation in order to stabilize the wing and reduce the effect of gust loadings. This assumption simplifies the design of the control system and marks

the first step in the right direction toward understanding and building active aeroelastic controls for wings with multiple ailerons.

However, implementing an active aeroelastic control on a given wing needs actuators. The dynamics of the actuators has great influence on the overall system performance. The first attempt toward including actuators' dynamics in the control system design was in 2016 (Singh et al., 2016). Therein, a receptance-based controller was designed for a wing with a leading and trailing control surface and the control gains required to place the closed-loop poles at prescribed locations were computed by solving a set of nonlinear equations in the least-square sense. However, an optimal design of cascade active aerostatic controls for the wing and ailerons and actuators in multi-objective settings has not been investigated yet. The main goal in this chapter is to develop an optimal cascade control system for an aircraft wing with a leading and trailing aileron driven by two electromagnetic actuators. The dynamics of the wing, control surfaces, and actuators are considered in the design. The cascade control system shown in Figure 13 consists of two control loops: outer and inner control loop. The outer control loop is applied to the wing and ailerons dynamics. The control surface rotation $\beta_d(s)$ is the output and the difference between the desired bending deformation of the wing at a certain point, $q_d(s) = 0$, and actual deformation, $q(s)$, is the input. The required aileron's deflection $\beta_d(s)$ is converted into the required rack-pinion movement $X_d(s)$. The inner control system which accepts $X_d(s)$ as its reference input, calculates the amount of control energy required to drive the actuator having transfer function $T(s)$, and brings the actual actuator output $X(s)$ to its desired value $X_d(s)$. The actual displacement of the rack-pinion gear is then transformed into the actual flab's deflection $\beta(s)$. In the following sections, the aeroelastic mathematical model of a wing having a leading and trailing control surface is explained, the dynamic model of an electromagnetic actuator is

introduced, a slider-crank mechanism used to transform the linear displacement from the actuator's gearbox to a rotation angle is introduced and the concern equations are derived, description of the inner and outer control system is delineated, multi-objective design of the multi-loop control system with three objectives:1) minimization of energy consumption, 2) the inner closed-loop control must be faster than the outer one to prevent the propagation of the actuator disturbance, $D_a(s)$, to the system, and 3) the outer closed-loop should fast reject external gust loadings $w_g(s)$, is formulated. The selected design Objectives target three of the most important requirements in active aeroelastic controls that are related to the closed-loop system speed of response, energy saving, and robustness against external disturbances. Discssion of the results concludes this chaper.

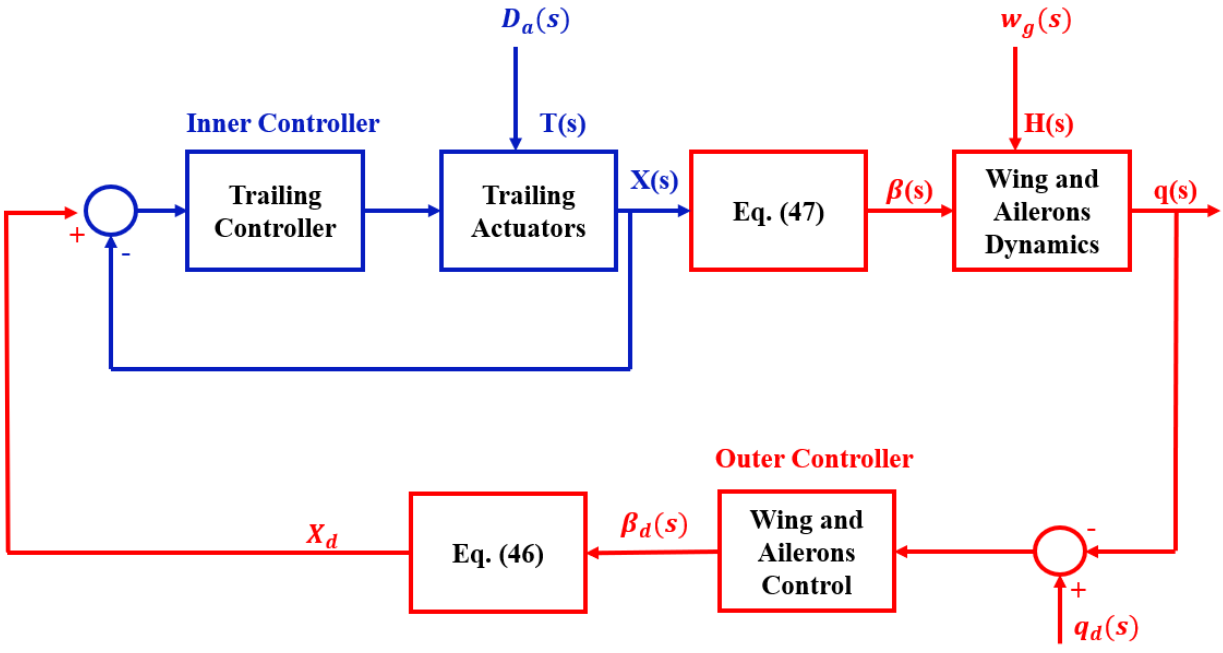

Figure 13: Cascade control system of aeroelastic structure and actuators

3.2 Airfoil wing model with two control surfaces

An aircraft wing model with a leading and trailing control surface is shown in Figure 14 (Singh et al., 2016). The system's dynamics reads

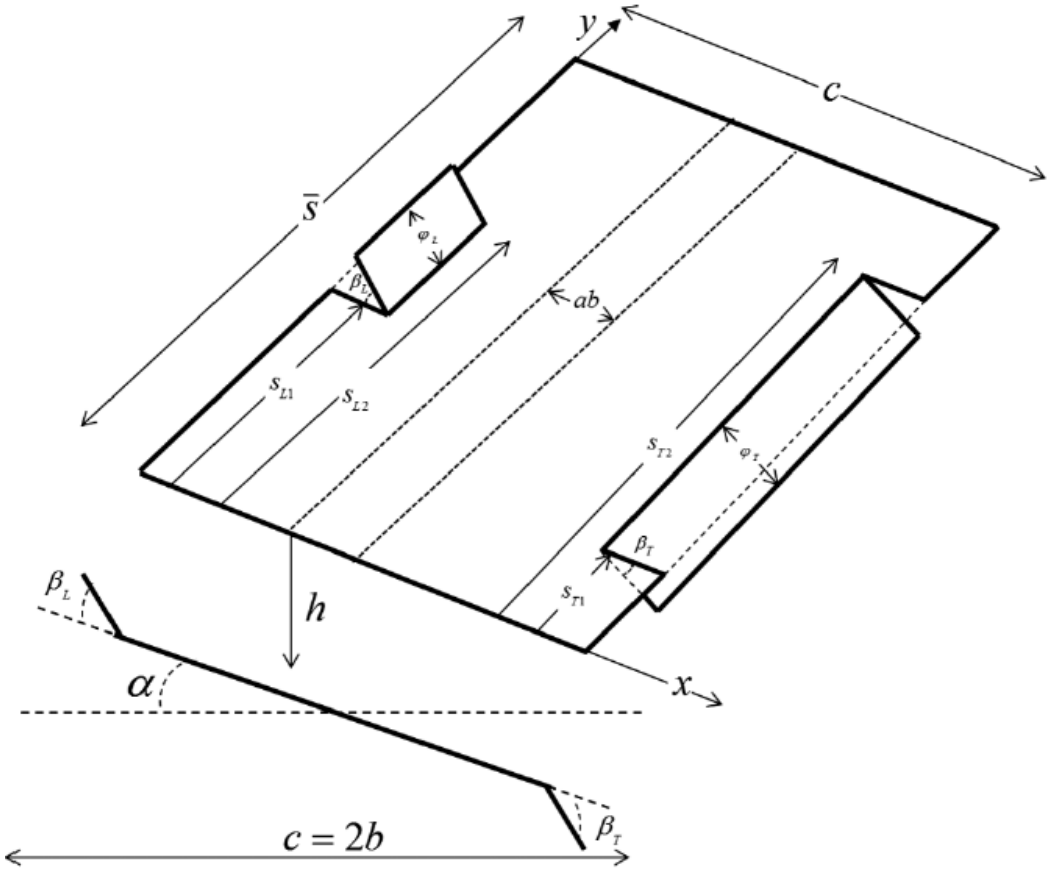

Figure 14: Airfoil wing model with two control surfaces (Singh et al., 2016).

$$\boldsymbol{M}\ddot{\boldsymbol{q}}(t) + \boldsymbol{C}(V)\dot{\boldsymbol{q}}(t) + \boldsymbol{K}(V)\boldsymbol{q}(t) = \boldsymbol{B}_{cs}\boldsymbol{\beta}_d(t) + \boldsymbol{B}_{ad}\boldsymbol{w}_g(t). \quad (28)$$

Among them, ***M***, ***C***, *and* $\boldsymbol{K} \in \Re^{n\times n}$ are respectively the inertia, equivalent damping (structural and velocity dependent aerodynamic damping), and equivalent stiffness (structural and velocity dependent aerodynamic stiffness) matrices. The vector $\boldsymbol{q}(t) = [h \quad \alpha]^T$ represents the degree of freedom of the structure where *h* is the plunging displacement (positive downward) and α is the pitching angle (positive nose up). $\boldsymbol{\beta}_d(t) \in \Re^{m\times 1}$ is the desired control deflection supplied by the

m number of control surfaces; $\boldsymbol{B}_{cs} \in \Re^{n\times m}$is the control distribution matrix representing the location and aerodynamic loading of control surfaces; and $\boldsymbol{B}_{ad} \in \Re^{n\times m}$ is the matrix describing the influence of the aerodynamic load, $\boldsymbol{w}_g$ (t), on the system. The term $\boldsymbol{B}_{ad}\boldsymbol{w}_g(\boldsymbol{t})$ was added to investigate the impact of the aerodynamic loads on the closed-loop and open-loop system performance. The values of $\boldsymbol{B}_{ad}$ were found by comparing the elements of the control distribution matrix $\boldsymbol{B}_{cs}$ and the aerodynamic load distribution matrix $\boldsymbol{B}_{ad}$ for the system proposed in (Kumar et al., 2012b) with those of the model at hand. A detailed description of the model with parameters' definitions and values used in the computer simulations can be found in Appendix B.

The system in Eq. (28) can be written as

$$\ddot{\boldsymbol{q}}(t) = -\boldsymbol{M}^{-1}\boldsymbol{C}(V)\dot{\boldsymbol{q}}(t) - \boldsymbol{M}^{-1}\boldsymbol{K}(V)\boldsymbol{q}(t) + \boldsymbol{M}^{-1}\boldsymbol{B}_{cs}\boldsymbol{\beta}_d(t) + \boldsymbol{M}^{-1}\boldsymbol{B}_{ad}\boldsymbol{w}_g(t). \quad (29)$$

The state equation of Eq. (29) in a matrix form reads

$$\dot{\boldsymbol{x}}(t) = \boldsymbol{A}\boldsymbol{x}(t) + \boldsymbol{B}\boldsymbol{\beta}_d(t) + \boldsymbol{B}_g\boldsymbol{w}_g(t), \quad (30)$$

$$\boldsymbol{y}(t) = \boldsymbol{C}_o\boldsymbol{x}(\boldsymbol{t}), \quad (31)$$

The state vector, $\boldsymbol{x}(t)$, the state-space dynamic matrix **A**, the input matrices **B** and $\boldsymbol{B}_g$, and the output matrix $\boldsymbol{C}_o$ are given by,

$$\boldsymbol{x}(t) = \begin{bmatrix} h \\ \alpha \\ \dot{h} \\ \dot{\alpha} \end{bmatrix}, \quad (32)$$

$$\mathbf{A} = \begin{bmatrix} \mathbf{0}_{2\times2} & \boldsymbol{I}_{2\times2} \\ -\boldsymbol{M}_{2\times2}^{-1}\boldsymbol{K}(V) & -\boldsymbol{M}_{2\times2}^{-1}\boldsymbol{C}(V) \end{bmatrix}, \quad (33)$$

$$\mathbf{B} = \begin{bmatrix} \mathbf{0}_{2\times2} \\ -\boldsymbol{M}_{2\times2}^{-1}\boldsymbol{B}_{cs} \end{bmatrix}, \tag{34}$$

$$\boldsymbol{B}_g = \begin{bmatrix} \mathbf{0}_{2\times2} \\ -\boldsymbol{M}_{2\times2}^{-1}\boldsymbol{B}_{ad} \end{bmatrix}, \tag{35}$$

$$\boldsymbol{C}_o = [\boldsymbol{I}_{2\times2} \quad \mathbf{0}_{2\times2}], \tag{36}$$

here, **I** and **0** denote the identity and zero matrices, respectively. This realization of the wing's dynamics and its leading and trailing ailerons is very useful in the control design of the outer control loop. The state-space model is used in the next section to design an optimal outer control algorithm.

3.3 LQR-based Outer Control Loop

A MIMO full-state feedback control law that calculates the desired deflection for the trailing and leading ailerons for the aircraft's wing represented by the state-space system given in Eq. (30) can be written as

$$\boldsymbol{\beta_d}(t) = -\mathbf{K}_\mathbf{C}\mathbf{x}(t), \tag{37}$$

The state feedback gain matrix $\mathbf{K_C}$ can be designed in different ways. One of the popular methods in classical optimal control is the Linear Quadratic Regulator (LQR). The optimal state feedback control gain matrix $\mathbf{K_C}$ can be obtained by minimizing the following performance index:

$$\mathrm{J} = \int_0^\infty [\mathbf{x}^T(t)\mathbf{Q}\mathbf{x}(t) + \mathrm{u}^T(t)\mathbf{R}\mathrm{u}(t)]\, dt, \tag{38}$$

where $\mathbf{Q} = \mathbf{Q}^\mathrm{T}$ is a positive semidefinite matrix that penalizes the departure of system states from the equilibrium, and $\mathbf{R} = \mathbf{R}^\mathbf{T}$ is a positive definite matrix that penalizes the control input. Using Lagrange multiplier-based optimization method, the optimal $\mathbf{K_C}$ is given by

$$\mathbf{K}_\mathrm{C} = \mathbf{R}^{-\mathbf{1}}\boldsymbol{BP} \tag{39}$$

The matrix $\boldsymbol{P} \in \Re^{4\times 2}$ can be calculated by solving the following Algebraic Riccati Equation (ARE):

$$\mathbf{A}^{\mathrm{T}}\mathbf{P} + \mathbf{P}\mathbf{A} - \mathbf{Q} - \mathbf{P}\mathbf{B}\mathbf{R}^{-1}\mathbf{B}^{\mathrm{T}}\mathbf{P} = \mathbf{0} \tag{40}$$

By examining Eqs. (39) and (40), we can notice that the weighting matrices **Q** and **R** play an important role in the LQR optimization process. That is, the elements of the **Q** and **R** matrices affect greatly the performance of a closed-loop system. Thus, the most important step in the design of an optimal controller using LQR is the choice of **Q** and **R** matrices. Conventionally, these matrices are elected based on the designer's experience and adjusted iteratively to obtain the desired performance. Arbitrary selection of **Q** and **R** will result in a certain system response which is not optimal in true sense. Many efforts have been directed toward developing systematic methods for selecting the weighting matrices. For instance, Bryson presented an approach for choosing the starting values of **Q** and **R** matrices, but this method only suggests the initial values and later the coefficients are to be tuned iteratively for optimal performance (Bryson, 2018). Hence, an optimization algorithm is needed to tune the elements of these matrices such that the desired response is achieved. Analytical ways of selecting the **Q** and **R** matrices for a second order crane system were developed by Oral et al. (2010). Another analytical method of calculating the **Q** and **R** matrices for a third order system represented in the control canonical form was proposed by El Hajjaji and Ouladsine (2001). Developing an analytical technique to find **Q** and **R** for high order systems such as the system at hand is very tedious, if it is not possible because of the dimension of the system and the number of design objectives that need to be achieved simultaneously. Therefore, we suggest a numerical approach through using an optimization algorithm to tune these matrices such that the design goals are optimized simultaneously.

The LQR does not only guarantee the system stability but also the stability margins (Chen, 2015). This feature is very valuable for high-order dynamic systems such as the mathematical model at hand where finding the feasible regions of the control gains is very difficult. On the other side, LQR requires that you have a good model of the system, and all the states in the system are available for feedback. If not all the states are available, an observer should be used to estimate the unavailable ones. As a result, stability margins may get arbitrarily small. Furthermore, LQR is based on state-space model of the system which doubles the system dimension as shown in Eq. (29).

In this work, LQR is used to calculate the feedback matrix $\mathbf{K}_C$ through optimally adjusting **Q** and **R**. One of the objectives that were considered in the optimization is the alleviation of the gust loading and minimization of the required control energy. To quantitively describe these objectives, the control law in Eq. (37) is first substituted in Eq. (30)

$$\dot{\boldsymbol{x}}(t) = \boldsymbol{A}\boldsymbol{x}(t) + \boldsymbol{B}[-\mathbf{K}_C\boldsymbol{x}(t)] + \boldsymbol{B}_g\boldsymbol{w}_g(t), \tag{41}$$

which can be simplified into

$$\dot{\boldsymbol{x}}(t) = (\boldsymbol{A} - \boldsymbol{B}\boldsymbol{K}_C)\boldsymbol{x}(t) + \boldsymbol{B}_g\boldsymbol{w}_g(t), \tag{42}$$

Taking the Laplace of Eq. (42) and simplifying, we obtain

$$\mathbf{x}(\mathrm{s}) = (s\boldsymbol{I} - \boldsymbol{A} + \boldsymbol{B}\boldsymbol{K}_C)^{-1}\boldsymbol{B}_g\boldsymbol{w}_g(t), \tag{43}$$

Taking the Laplace of Eq. (31) and substituting with Eq. (43), we get

$$\mathbf{y}(\mathrm{s}) = \boldsymbol{C}_o(s\boldsymbol{I} - \boldsymbol{A} + \boldsymbol{B}\boldsymbol{K}_C)^{-1}\boldsymbol{B}_g\boldsymbol{w}_g(t), \tag{44}$$

From this equation, the transfer function matrix $\boldsymbol{GTF}(\boldsymbol{s})$ from the gust loads to the system's outputs is provided by

$$\boldsymbol{GTF}(\boldsymbol{s}) = \frac{\mathbf{y}(\mathrm{s})}{\boldsymbol{w}_g(t)} = \boldsymbol{C}_o(s\boldsymbol{I} - \boldsymbol{A} + \boldsymbol{B}\boldsymbol{K}_C)^{-1}\boldsymbol{B}_g\boldsymbol{w}_g(t), \tag{45}$$

Eq. (45) describes the effect of measurement noise and external gust loads on the system performance. This is a very important objective in the control system design of aeroelastic structures. It is obvious from this equation that large $\boldsymbol{K_C}$ values are required in order to reduce the effect of aerodynamic loadings. In the same time, large $\boldsymbol{K_C}$ values mean high energy consumption. Since the controlled system is optimized for zero initial conditions, the control energy $\boldsymbol{E_s}$ cannot be included directly in the objective function and its Frobenius norm is used instead. By minimizing this norm, the control energy is also minimized (Singh & McDonough, 2014). In mathematical terms, the Frobenius norm of the control matrix is given by

$$E_s = \sum_{i=1}^{2} \sum_{j=1}^{4} k_{ij}, \tag{46}$$

where $k_{ij}$are the elements of feedback gain matrix, $\boldsymbol{K_C}$ calculated from Eq (39).

In real applications, actuators are used to derive the control surfaces and deliver the desired deflection, $\boldsymbol{\beta}_d(t)$**.** The structure of these actuators is usually complicated and involves a control system, amplifier circuit, motor, gear train, and slider-crank mechanism. In the next section, we describe these components and pay more attention to the control system design.

3.4 Actuator Dynamics

Hydraulic actuators (HA) are widely used in aircrafts such as A380 and G650 (Derrien & Sécurité, 2012). However, modular electro-mechanical actuators (EMAs) have been increasingly replacing hydraulic actuators in the aerospace sector in the past decade. Smaller weight, better energy efficiency, and the availability of the EMAs are the main motivations for this replacement (Habibi et al., 2008). For this reason, an EMA is chosen as a driver for the leading and trailing control surface of the wing shown in Figure 14. A pictorial depiction of a generic EMA system is shown in Figure 15. The EMA actuator consists of a control system (inner loop), high performance brushless DC motor, and ball gear, and mechanical linkage (see Figure 16).

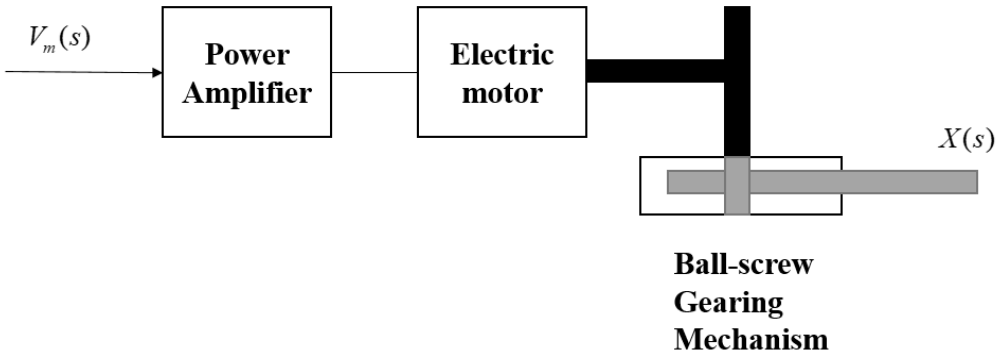

Figure 15: A generic EMA system (Habibi et al., 2008)

The model of the DC motor is well established and presented here in a summarized form (Habibi et al., 2008). The system parameters needed to simulate this system are listed in Table 1 of Appendix B. The mathematical model that relates the gear-ball position X with its input voltage V_m reads

$$G_a = \frac{X}{V_m} = \frac{K}{s(\tau s+1)}, \quad (47)$$

where, V_M is the motor input voltage, X is the position of the ball-screw mechanism, $K = 0.0452$ is the DC gain of the motor, and $\tau = 0.0026$ is the time constant. A detailed description of the EMA equations can be found in Appendix B. The linear displacement X from the ball-screw mechanism is used as an input to the slider-crank mechanism shown in Figure 16. As shown in Figure 13, Given the desired control surface deflection $\boldsymbol{\beta}_d(t)$, the required movement $\boldsymbol{X}_d(t)$, of the ball-screw mechanism can be calculated from Eq. (48). Also, if the actual displacement *X* of the gear-ball mechanism is measured, the actual rotational angle $\boldsymbol{\beta}(t)$ of the flab can be found from Eq. (49).

$$\mathbf{X_d} = a\,[n\left(1 - \sqrt{1 - \frac{\sin \boldsymbol{\beta_d}(t)^2}{n^2}}\right) + (1 - \cos \boldsymbol{\beta_d}(t))]. \quad (48)$$

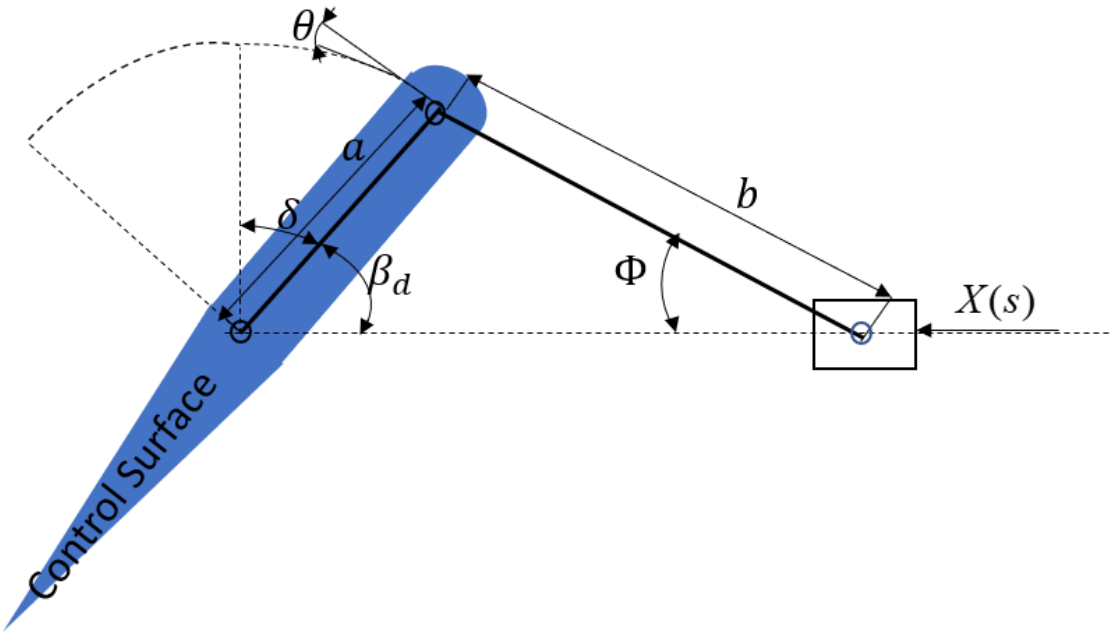

Figure 16: Control surface driven by slider-crank mechanism

$$\boldsymbol{\beta}(t) = \arccos\frac{(1+n-\frac{X}{a})^2-n^2+1}{2\ (1+n-\frac{X}{a})}. \quad (49)$$

Where, $n = \frac{b}{a}$, the length of crank a=100 mm; the length of linkage b =170 mm. In Figure 16, Φ is the angle between the linkage and horizontal line in pivoting. A detailed derivation of Eq. (48) and Eq. (49) can be found in Appendix B.

3.5 PV-based Inner Control Loop

The dynamics of the actuators has great impact on the performance of the closed-loop dynamics of the aeroelastic system. In the following, we assume that the trailing and leading flaps are driven by two identical actuators that are modeled by Eq. (47). From this equation, the dynamics of the actuator in form of a differential equation reads

$$\tau\ddot{X} + \dot{X} = KV_m \ . \quad (50)$$

Assuming the existence of an external load disturbance labeled $D_a(t)$ as shown in Figure 13, this equation can be modified to

$$\tau\ddot{X} + \dot{X} = K(V_m(t) + D_a(t)). \quad (51)$$

Since the system inherently has an integrator, a PV (Proportional-Velocity) controller is enough to stabilize the system and provide good tracking. The control law reads

$$V_m(t) = k_p(X_d(t) - X(t)) - k_v\dot{X}(t) \ . \quad (52)$$

Substituting Eq. (52) into Eq. (51), we obtain

$$\tau\ddot{X} + \dot{X} = K\big(k_p(X_d(t) - X(t)) - k_v\dot{X}(t) \ + D_a(t)\big) \quad (53)$$

Taking Laplace transformation and simplifying, we get

$$X(s) = \frac{Kk_p}{\tau s^2+(1+Kk_v)s+Kk_p} X_d(t) + \frac{K}{\tau s^2+(1+Kk_v)s+Kk_p} D_a(s) \quad (54)$$

Since there are two actuators, the subscript T and L will be used respectively to describe the closed-loop dynamics of the trailing and leading actuators that show the relationship between the actual and the desired ball-screw mechanism displacement, and effect of the load disturbance on the controlled system performance as follows

$$X_T(s) = \frac{Kk_{p_T}}{\tau s^2+(1+Kk_{v_T})s+Kk_{p_T}} X_{d_T}(t) + \frac{K}{\tau s^2+(1+Kk_{v_T})s+Kk_{p_T}} D_{a_T}(s), \quad (55)$$

$$X_L(s) = \frac{Kk_{p_L}}{\tau s^2+(1+Kk_{v_L})s+Kk_{p_L}} X_{d_L}(t) + \frac{K}{\tau s^2+(1+Kk_{v_L})s+Kk_{p_L}} D_{a_L}(s), \quad (56)$$

here, $X_T(s)$ and $X_L(s)$ are the actual displacement of ball-gear mechanism of the trailing and leading actuator, respectively. Similarly, $X_{d_T}(t)$ and $X_{d_L}(t)$ are used to denote the desired movements of these actuators. The parameters k_{p_T}, k_{v_T} , k_{p_L}, and k_{v_L}represent the adjustable gains of the trailing and leading control algorithms. The external excitation at the trailing and leading actuators are respectively $D_{a_T}(s)$ and $D_{a_L}(s)$. One of the main objectives in the design

of cascade controllers is to reduce the effect of these upsets. As a result, this effect needs to be quantified. Using the superposition principle, setting $X_{d_T}(t) = 0$ and $X_{d_L}(t) = 0$, and simplifying Eq. (55) and Eq. (56), we get

$$TF_{D_{a_T}}(s) = \frac{X_T(s)}{D_{a_T}(s)} = \frac{K}{\tau s^2 + (1 + K k_{v_T})s + K k_{p_T}}, \quad (57)$$

$$TF_{D_{a_L}}(s) = \frac{X_L(s)}{D_{a_L}(s)} = \frac{K}{\tau s^2 + (1 + K k_{v_L})s + K k_{p_L}}, \quad (58)$$

Another important objective in the design of cascade control loops is the speed of response of the inner control system which can be characterized from the closed-loop character equations of both leading and trailing control algorithms which are given by

$$CE_T = \tau s^2 + (1 + K k_{v_T})s + K k_{p_T} \quad (59)$$

$$CE_L = \tau s^2 + (1 + K k_{v_L})s + K k_{p_L} \quad (60)$$

Also, the control energy expenditure of the trailing and leading actuators can be quantified by using the Frobenius norm of the control parameters as follows

$$E_T = \sqrt{k_{p_T} + k_{d_T}}, \quad (61)$$

$$E_L = \sqrt{k_{p_L} + k_{d_L}}, \quad (62)$$

Having all the objectives defined and all the tuning parameters specified, the multi-objective optimization can be now setup.

3.6 Multi-objective and Multidisciplinary Optimal Design

The design parameter space **k** including tunable parameters of the outer and inner controller is given by,

$$\boldsymbol{k} = \left[Q_1, Q_2, Q_3, Q_4, R_1, R_2, k_{p_T}, k_{d_T}, k_{p_L}, k_{d_L}\right] \quad (63)$$

The parameters $Q_1, \ldots, Q_4$ are the diagonal elements of the state weighting matrix (**Q**), and R_1, R_2 are the elements on the diagonal of the control weighting matrix (**R**). These design knobs are used to indirectly tune the full-state feedback vector gain, $\mathbf{K_C}$, while, $k_{p_T}, k_{d_T}, k_{p_L}$ and k_{d_L} are the setup parameters of the inner control algorithms applied to the actuators driving the trailing and leading control surfaces. The control and geometrical constraints on these setup parameters are defined as follows:

$$\boldsymbol{D} = \begin{Bmatrix} \boldsymbol{k} \in \mathfrak{R}^{10} \mid Q_1, Q_2, Q_3, Q_4 \in [0{,}100], \\ R_1 \text{and } R_2 \in [0.001{,}100], \\ k_{p_T} \text{and } k_{p_L} \in [0.1{,}100], \\ k_{d_T} \text{and } k_{d_T} \in [-22{,}10]. \end{Bmatrix} \tag{64}$$

The upper limits for all the parameters were arbitrarily chosen. The ranges for $k_{p_T}, k_{d_T}, k_{p_L}$ and k_{d_L} were chosen according to stability constraint required by Eq. (59) and Eq. (60). These parameters were optimally tuned by minimizing the following design objectives

$$\min_{\boldsymbol{k} \in \boldsymbol{D}} \{-r, D_{av}, E_{av}\}, \tag{65}$$

here *r* defines the relative speed of the inner controlled systems with respect to the outer control loop and it is defined by

$$r = \lambda_a \backslash \lambda_s, \tag{66}$$

where λ_a is the dominant closed-loop pole from the two inner control algorithms and λ_s is the dominant pole from the aeroelastic structure under the LQR- based controller and they are given by

$$\lambda_a = max[max\big(real(CE_T)\big)\ max(real(CE_T))] \tag{67}$$

$$\lambda_s = max\big(real(\mathbf{A} - \mathbf{BK_C})\big) \tag{68}$$

The *real* function denotes the operation that extracts the real parts from the closed-loop eigenvalues while *max* is the math operator that returns the dominant poles. It is worth noting

that big values of *r* indicate highly responsive inner control algorithms compared to the outer control loop. The disturbance affecting the controller in the inner and outer paths can be described by

$$D_{av} = \frac{1}{3}\left(\|\boldsymbol{GTF}(j\omega)\|_{\omega\in[\omega_1,\omega_2]} + \left\|TF_{D_{a_T}}(j\omega)\right\|_{\boldsymbol{\omega\in[\omega_3,\omega_4]}} + \left\|TF_{D_{a_L}}(j\omega)\right\|_{\boldsymbol{\omega\in[\omega_3,\omega_4]}} \right), \quad (69)$$

where $\boldsymbol{GTF}(j\omega)$, $TF_{D_{a_T}}(j\omega)$, and $TF_{D_{a_L}}(j\omega)$ are the functions defined in Eq. (45), Eq. (57), and Eq. (58), respectively, after replacing **s** with $j\omega$. The values ω_1 and ω_2 are set to 0 and 1000, respectively, as suggested in (Singh et al., 2014). Finally, the total control energy from the outer and inner control loops is

$$E_{av} = \frac{1}{3}(E_S + E_T + E_L). \quad (70)$$

The definition of $E_S, E_T,$ and E_L were introduced in Eq. (46), Eq. (61), and Eq. (62).

To solve this multi-objective optimization problem having the cost functions defined in Eq. (65) and the setup parameters listed in Eq. (63) subjected to the constraints of Eq. (64), the nondominated sorting genetic algorithm (NSGA-II) is used. Readers are encouraged to refer to chapter 1.3 of this thesis or consult Deb's book titled "Multi-Objective Optimization Using Evolutionary Algorithms" (Deb, K., 2001) for more details about this algorithm. There is no specific guide on how to set up the number of populations and generations for this algorithm. However, according to the Matlab documentation, the population size can be set in different ways and the default population size is 15 times the number of the design variables *n*. Also, the maximum number of generations should not be greater than $200 \times n$. In this study, the population size is set to 50×10, and the number of generations is set to 500. The solution of this problem results in a set of solutions called Pareto set and the set of the corresponding

function evaluation is called Pareto front. The next section sheds more light on the optimization results.

3.7 Results and Discussion

The Pareto front, Pareto set, and dynamics of the controlled system states versus time are discussed here.

3.7.1 Pareto Frontier and Set

The Pareto Front representing the objective space is shown in Figure 17. The top portion of this figure shows the change of E_{av} versus D_{av} and the varying of the color portrays the level of E_{av}, where the blue and red colors correspond to the lowest and highest values, respectively. As is evident from this plot, there is non-agreement relationship between the objective of maximizing the capacity of the controlled system to reject external upsets and that of minimizing the amount of control energy. For example, when $D_{av} = 0.1157$ (best disturbance rejection), the average control energy is 31.8497, while, E_{av} is only 14.1641 at $D_{av} = 0.3926$ (worst disturbance rejection). That is, the objective of minimizing the energy expenditure is conflicting with that of improving the disturbance repudiation of the closed-loop system.

The bottom subplot of Figure 17 shows another conflicting relationship between E_{av} and r (the ratio of the dominant actuators' pole under the inner control algorithms to the dominant eigenvalue of the aeroelastic structure under the outer control system). High Energy levels are required in order to ensure that the slave controlled systems are faster than the master controlled loop. For instance, when the secondary controlled system is almost 50 times faster than the primarily closed-loop system ($r = 49.9382$), E_{av} is 30.5979. On the other side at $r = 1.2403$, E_{av} reads only 12.93. Many other design options can be found between these two extreme points

as shown in the figure. For instance, increasing the E_{av} from 12.93 to 14.1641, r goes up from 1.2403 to 11.3589. That is, a small sacrifice in the control energy can significantly speed up the response of the inner controlled system compared to the outer one.

Different projections from the Pareto set are shown in Figures 18, 19, and 20. To show the corresponding design parameters for each point in the Pareto front, the color in these figures were also mapped to the value of E_{av}. It is evident from the color code in Figure 18 that a large control energy is associated with big control gains. Also, small values of R_1 and R_2 result in large control force because we put less weight on the importance of the control energy. On other side, large values of R_1 and R_2 result in small control force because we put more emphasis on the minimization of the control energy as shown in Figure 20.

The effect of the state weighting parameters, $Q_1, \ldots, Q4$, on the value of the control signal is shown in Figure 19. The figure confirms the importance of tuning these knobs and their noticeable impact on the energy required to derive the system. Different energy levels can be obtained by changing these gains as shown in the figure.

3.7.2 Closed-Loop Eigenvalues

One of the important objectives in the design of cascade controller is to make the response of the inner control loop faster than that of the outer. To this end, the dominant pole of the subsystem controlled by the slave control algorithm should be placed to the left of that of the plant driven by the master control loop. This was represented in the objective space by the cost function *r*. Figure 21 shows the closed-loop poles' locations of the aeroelastic structure under the outer controller, trailing actuator controlled by an inner PV-based controller, and leading actuator driven also by another PV-based control. The color code in this figure is also mapped to the

value of the average control energy. By inspecting this figure, we can notice that the dynamics of the aeroelastic structure dominates that of the trailing and leading actuators. This can be also confirmed by inspecting Figure 22 which focuses only on the real part of the dominant poles. Here, λ_a is the dominant pole from the two actuators. Comparing the values on the x-axis of Figure 22-a with that of Figure 22-b, we notice that actuators will always act faster than the aeroelastic structure to prevent the propagation of external disturbance to the aircraft's wing.

3.7.3 Gust Loading Impact

For the velocity, V=11.4 m/s (onset of flutter), the closed loop response of the aeroelastic structure, trailing actuator, and leading actuator were computed when they are excited by a discrete "1-cosine" gust loading, which is given by

$$w_g(t) = \frac{\overline{w_g}}{2}\left(1 - cos\frac{2\pi t}{L_g}\right) \; for \;\; 0 < t < L_g. \tag{71}$$

Among them, $\overline{w_g}$ is the maximum gust velocity, and L_g is the total length of gust bump. Following the work proposed by Haghighat et al. (2012), we set, $\overline{w_g}$ and L_g respectively to $4.575\ m/s$, and $0.5\ s$. The profile of the gust load over time is shown in Figure 23. The profile shows a sudden spike in the first half second.

The closed-loop system response shows very small tracking error (TE) as labelled on the figure when the disturbance rejection is high (see Figure 24), the control energy is large (see Figure 26), and the secondary control algorithms are way faster than primary one (see Figure 28). This behavior is expected since small D_{av}, high E_{av}, or large r are required for better tracking. On other side, large values of D_{av}, small levels of E_{av}, or small r values will result in large tracking error as shown in Figure 25, 27, and 29, respectively. In fact, when E_{av} is at lowest level, the tracking is very bad and the system tends to continuously oscillate over time as

depicted in Figure 27. Furthermore, if the inner loops do not act quickly to eliminate the impact of the gust loading, the controlled system will be also oscillatory as shown in Figure 29.

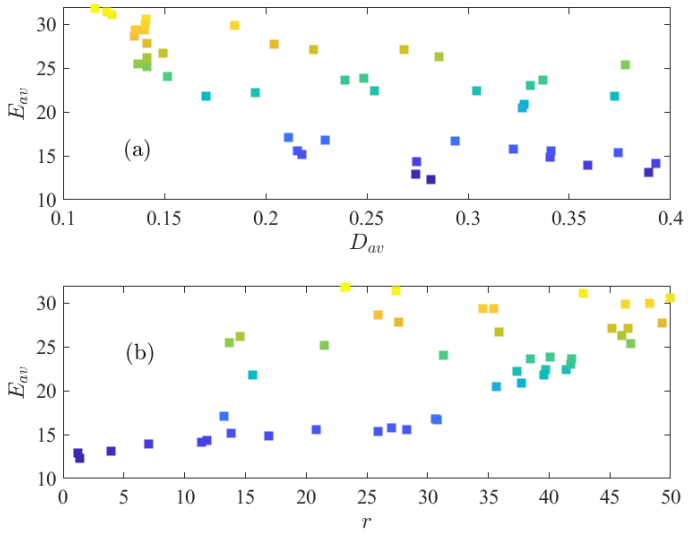

Figure 17: Projections of the Pareto front: (a) E_{av} versus D_{av}, (b) E_{av} versus r. The color code indicates the level of E_{av}, where red denotes the highest value, and dark blue denotes the smallest.

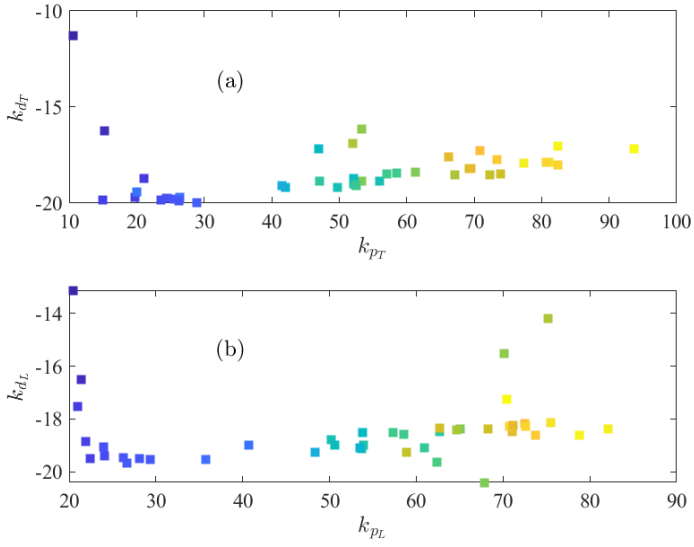

Figure 18: Projections of the Pareto set: (a) k_{pT} versus k_{dT} (b) k_{pL} versus k_{dL}. The color code indicates the level of E_{av}, where red denotes the highest value, and dark blue denotes the smallest.

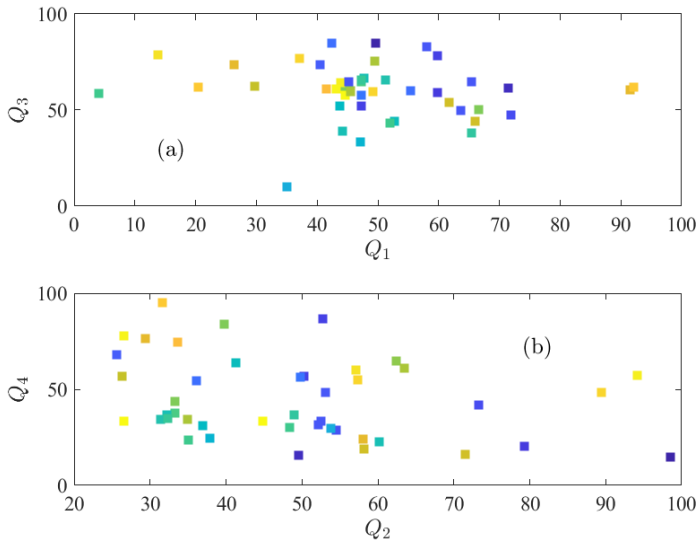

Figure 19: Projections of the Pareto set: (a) Q_1 versus Q_3 (b) Q_2 versus Q_4. The color code indicates the level of E_{av}, where red denotes the highest value, and dark blue denotes the smallest.

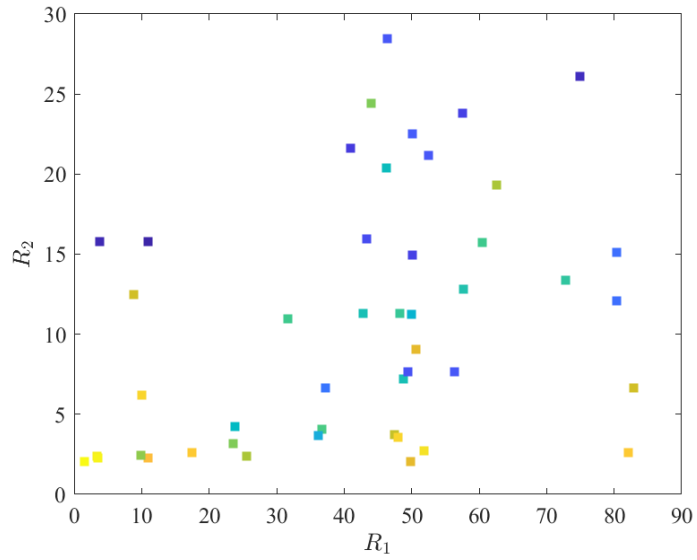

Figure 20: A Projection of the Pareto set: R_1 versus R_2. The color code indicates the level of E_{av}, where red denotes the highest value, and dark blue denotes the smallest.

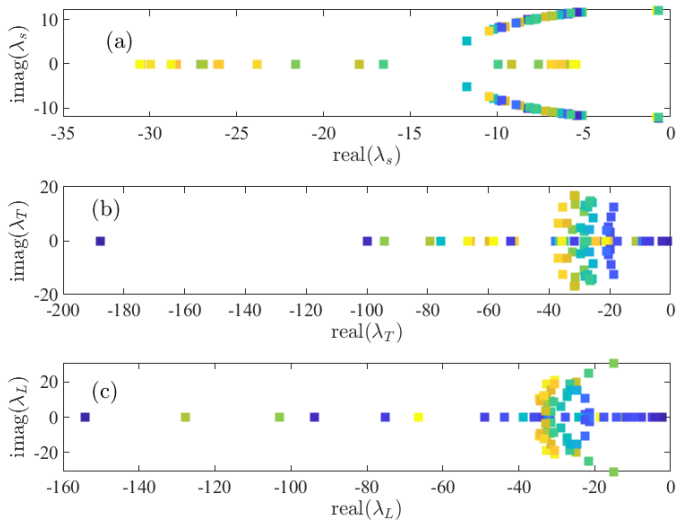

Figure 21: Pole maps, on the y-axis is the imaginary part of the pole, imag(λ), and the x-axis is the real part of the pole, real(λ): (a) Pole map of the outer controlled system: outer control loop and aeroelastic structure, (b) Pole map of the inner controller applied to the trailing actuator, and (c) Pole map of the inner controller applied to the leading actuator.

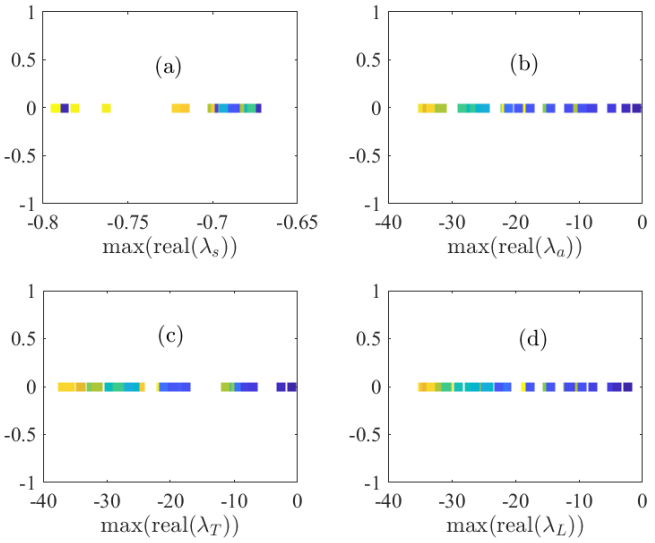

Figure 22: Dominant pole maps, the x-axis is the location of pole closer to the imaginary axis, max(real(λ)) the y-axis is unlabeled, and: (a) Dominant pole map of the outer controlled system: outer control loop and aeroelastic structure, (b) Dominant pole map of the trailing and leading inner controllers, (c) Dominant pole map of the inner controller applied to the trailing actuator, and (d) Dominant pole map of the inner controller applied to the leading actuator.

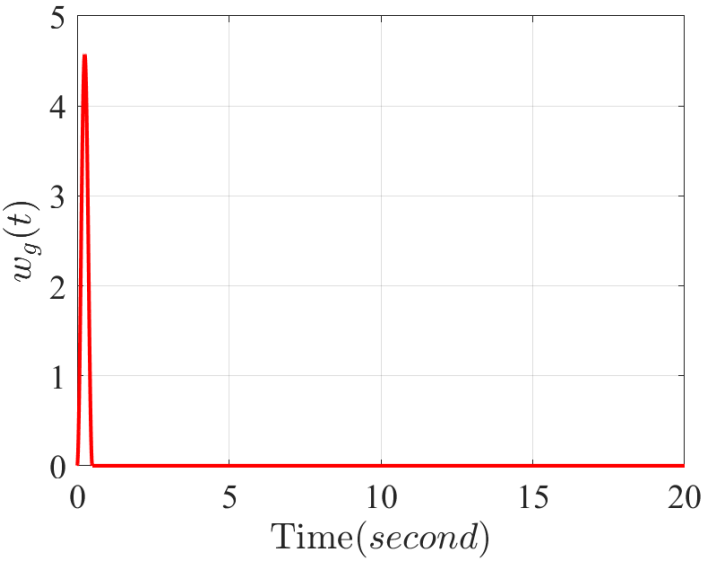

Figure 23:Gust load $w_g(t)$ profile versus time.

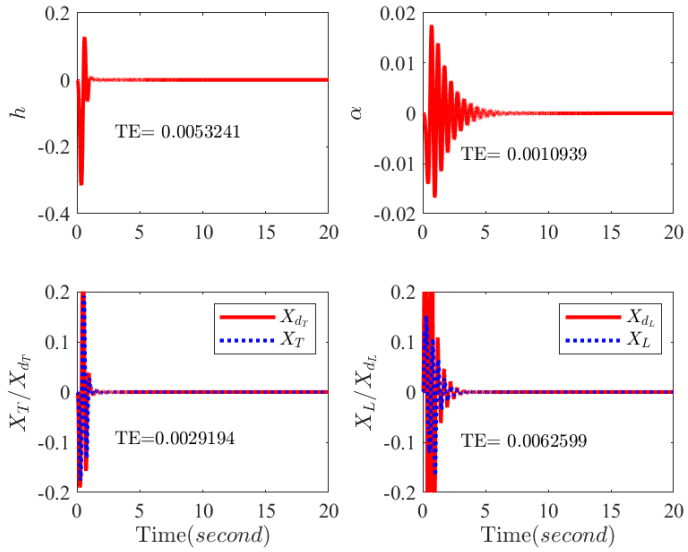

Figure 24: Controlled systems' responses when the disturbance rejection is the best min (D_{av}). Top left: time versus the plunging displacement (h). Top right: time versus the plunging the pitching angle α. Bottom left: time versus the actual X_T and desired X_{dT} ball-screw mechanism displacement of the actuator at the trailing aileron. Bottom Right: time versus the actual X_L and desired X_{dL} ball-screw mechanism displacement of the actuator at the leading aileron.

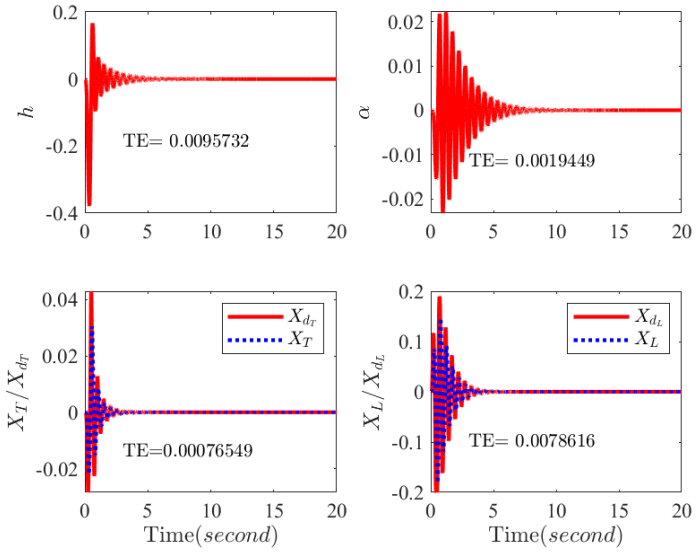

Figure 25: Controlled systems' responses when the disturbance rejection is the worst max (D_{av}). Top left: time versus the plunging displacement (h). Top right: time versus the plunging the pitching angle α. Bottom left: time versus the actual X_T and desired X_{dT} ball-screw mechanism displacement of the actuator at the trailing aileron. Bottom Right: time versus the actual X_L and desired X_{dL} ball-screw mechanism displacement of the actuator at the leading aileron.

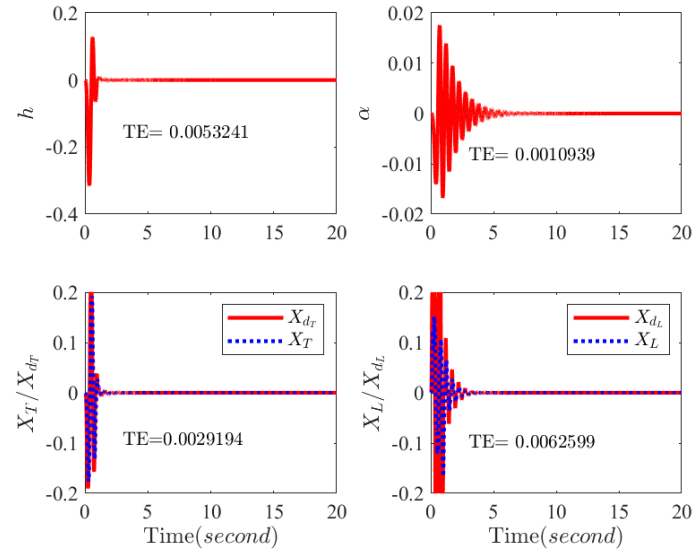

Figure 26: Controlled systems' responses when the control energy is the maximum max (E_{av}). Top left: time versus the plunging displacement (h). Top right: time versus the plunging the pitching angle α. Bottom left: time versus the actual X_T and desired X_{dT} ball-screw mechanism displacement of the actuator at the trailing aileron. Bottom Right: time

versus the actual X_L and desired X_{dL} ball-screw mechanism displacement of the actuator at the leading aileron.

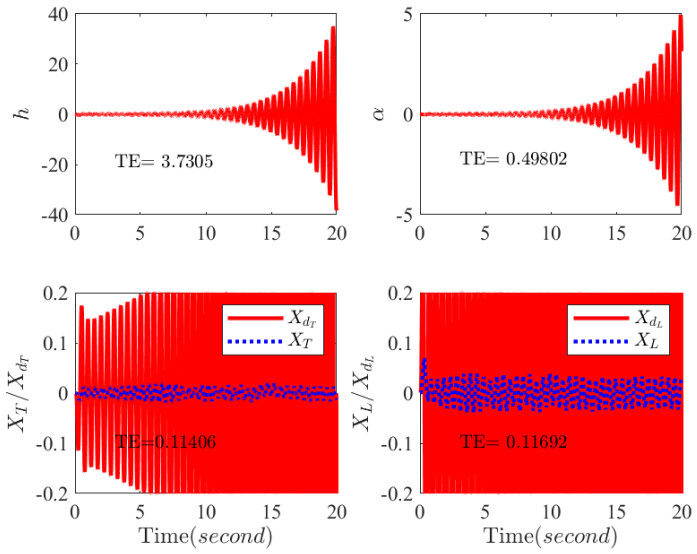

Figure 27: Controlled systems' responses when the control energy is the minimum min(E_{av}). Top left: time versus the plunging displacement (h). Top right: time versus the plunging the pitching angle α. Bottom left: time versus the actual X_T and desired X_{dT} ball-screw mechanism displacement of the actuator at the trailing aileron. Bottom Right: time versus the actual X_L and desired X_{dL} ball-screw mechanism displacement of the actuator at the leading aileron.

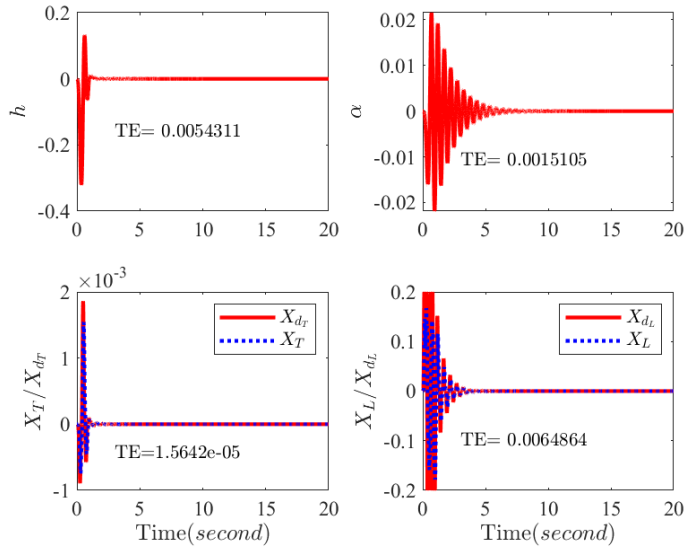

Figure 28: Controlled systems' responses when the inner closed-loop algorithms are way faster than outer control loop max (r). Top left: time versus the plunging displacement (h). Top right: time versus the plunging the pitching angle α. Bottom left: time versus the actual X_T and desired X_{dT} ball-screw mechanism displacement of the actuator at the trailing aileron. Bottom Right: time versus the actual X_L and desired X_{dL} ball-screw mechanism displacement of the actuator at the leading aileron.

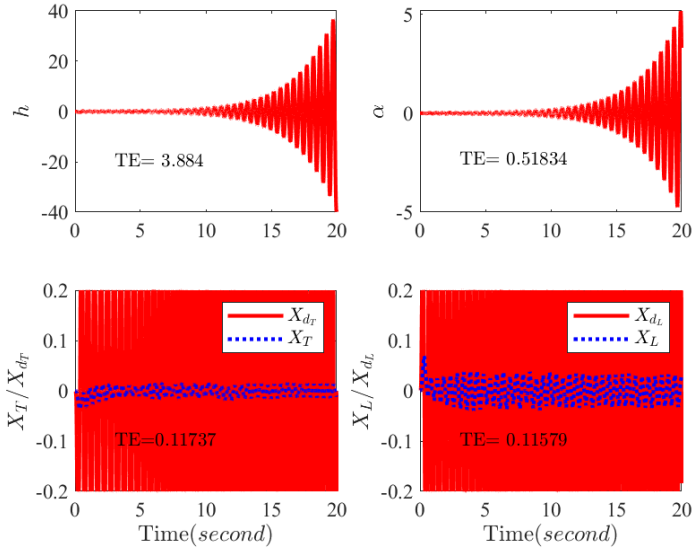

Figure 29: Controlled systems' responses when the inner closed-loop algorithms are way slower than outer control loop max (r). Top left: time versus the plunging displacement (h). Top right: time versus the plunging the pitching angle α. Bottom left: time versus the actual X_T and desired X_{dT} ball-screw mechanism displacement of the actuator at the trailing aileron. Bottom Right: time versus the actual X_L and desired X_{dL} ball-screw mechanism displacement of the actuator at the leading aileron.

CHAPTER 4: SUMMARY AND FUTURE DIRECTIONS

4.1 Conclusions

We have studied the multi-objective optimal design of a two cascaded controller based on two PD controllers. A numerical example which consists of a servo DC motor and ball-beam system is used. The optimization problem with four design parameters and four conflicting objective functions is solved with the NSGA-II algorithm. The Pareto set and front are obtained. The Pareto set includes multiple design options from which the decision-maker can choose to implement. The results show there are many optimal trade-offs among load disturbance rejection, measurement noise repudiation, control energy saving, tracking error reduction, and relative speed of response of the inner loop subsystem with respect to the outer one. Also, the pole maps of the control loops demonstrate that the inner closed-loop system has a faster dynamic than that of the outer controlled system.

We have also investigated the multi-objective optimal design of three cascaded controllers, two slave algorithms applied to the actuators and a master controller for the aircraft's wing. The outer algorithm is based on the optimal LQR algorithm while the inner loops are PV-based controllers. A numerical example which consists of an aircraft's flexible structure and two EMA actuators are used. The optimization problem with ten design parameters and three conflicting objective functions is solved with the NSGA-II algorithm. The Pareto set and front are obtained, and the results show inherit trade-offs among the design goals. The pole locations of the three subsystems clearly show that the inner closed-loop systems are faster than that of the outer controlled system.

4.2 Future Works

Future work will include designing an optimal and multidisciplinary cascade controller aeroelastic structures or aircraft wings with different number of ailerons. The design will include the controllers' gains as well as the geometrical parameters of the control surfaces. Also, the backlash effect on the ball-screw mechanism connected to the DC motor will be investigated. Furthermore, the dynamic of the slider-crank mechanism and its effect on the system behavior will be included in the future studies.

REFERENCES

Abdalla, M., Alsharif, M., Atkare, U., Bagwe, R., Boaks, M., Borkar, R., & Brown, D. (2016). DC Motor Drive System Cascade Control Strategy. *Engineering*.

Aerospaceweb. (2012, 02 24). Retrieved from http://www.aerospaceweb.org/question/aerodynamics/q0167.shtml

Agees Kumar, C., & Kesavan Nair, N. (2012). Multiobjective Cascade Control System Design with an application to Level Control in Liquid Level process. *Life Science Journal, 9*(3).

Alfaro, V. M., Vilanova, R., & Arrieta, O. (2008). Two-degree-of-freedom PI/PID tuning approach for smooth control on cascade control systems. *2008 47th IEEE Conference on Decision and Control*, (pp. 5680-5685).

Almutairi, N. B., & Zribi, M. (2010). On the sliding mode control of a ball on a beam system. *Nonlinear dynamics, 59*(1-2), 221.

Beyer, H. G., & Deb, K. (2001). On self-adaptive features in real-parameter evolutionary algorithms. *IEEE Transactions on evolutionary computation, 5*(3), 250-270.

Bhavina, R., Jamliya, N., & Vashishta, K. (2013). Cascade control of DC motor with advance controller. *International journal of Industrial Electronics and Electrical Engineering 1.1, 1*(1), 18-20.

Bryson, A. E. (2018). *Applied optimal control: optimization, estimation and control.* Routledge.

Chen, C. (2015). *On the robustness of the linear quadratic regulator via perturbation analysis of the Riccati equation.* Dublin City University: Doctoral dissertation.

Chen, C. Y., Hsu, C. H., Yu, S. H., Yang, C. F., & Huang, H. H. (2009). Cascade PI controller designs for speed control of permanent magnet synchronous motor drive using direct torque approach. *In 2009 Fourth International Conference on Innovative Computing, Information and Control (ICICIC), IEEE*, (pp. 938-941).

Chen, Z., Gao, W., Hu, J., & Ye, X. (2010). Closed-loop analysis and cascade control of a nonminimum phase boost converter. *IEEE Transactions on power electronics, 26*(4), 1237-1252.

Deb, K. (2001). Multi-objective optimization using evolutionary algorithms. *New York: John Wiley & Sons*, Vol. 16.

Deb, K., & Agrawal, R. B. (1995). Simulated binary crossover for continuous search space. *Complex systems, 9*(2), 115-148.

Deb, K., Pratap, A., Agarwal, S., & Meyarivan, T. A. (2002). A fast and elitist multiobjective genetic algorithm: NSGA-II. *IEEE transactions on evolutionary computation, 6*(2), 182-197.

Derrien, J.-C., & Sécurité, S. D. (2012). Electromechanical actuator (EMA) advanced technologies for flight controls. *In International Congress of the Aeronautical Sciences*, 1-10.

Dorf, R. C., & Bishop, R. H. (2011). Modern control systems. Pearson. *Pearson*.

Durillo, J. J., Nebro, A. J., Coello, C. A., García-Nieto, J., Luna, F., & Alba, E. (2010). A study of multiobjective metaheuristics when solving parameter scalable problems. *IEEE Transactions on Evolutionary Computation, 14*(4), 618-635.

Durillo, J. J., Nebro, A. J., Coello, C. A., Luna, F., & Alba, E. (2008). A comparative study of the effect of parameter scalability in multi-objective metaheuristics. *IEEE Congress on Evolutionary Computation (IEEE World Congress on Computational Intelligence)*, (pp. 1893-1900).

El Hajjaji, A., & Ouladsine, M. (2001). Modeling and nonlinear control of magnetic levitation systems. *IEEE Transactions on industrial Electronics, 48*(4), 831-838.

Franklin, G. F., Powell, J. D., Emami-Naeini, A., & Powell, J. D. (1994). Feedback control of dynamic systems. *Reading, MA: Addison-Wesley,* Vol. 3.

Franks, R., & Worley, C. (1956). Quantitative Analysis of Cascade Control. *Ind. and Eng. Chemistry, 48*(6), 1074-1079.

Fu, H., Pan, L., Xue, Y. L., Sun, L., Li, D. H., Lee, K. Y., & Zheng, S. (2017). Cascaded PI Controller Tuning for Power Plant Superheated Steam Temperature based on Multi-Objective Optimization. *IFAC-PapersOnLine, 50*(1), 3227-3231.

Gadhvi, B., Savsani, V., & Patel, V. (2016). Multi-objective optimization of vehicle passive suspension system using NSGA-II, SPEA2 and PESA-II. *Procedia Technology*, 23, 361-368.

Gaspari, A. D., Ricci, S., Riccobene, L., & Scotti, A. (2009). Active Aeroelastic Control Over a Multisurface Wing: Modeling and Wind-Tunnel Testing. *AIAA Journal*, 995-2010.

Habibi, S., Jeff, R., & Greg, L. (2008). Inner-loop control for electromechanical (EMA) flight surface actuation systems. *Journal of dynamic systems, measurement, and control*, 130(5), 051002.

Haghighat, S., Martins, J. R., & Liu, H. H. (2012). Aeroservoelastic design optimization of a flexible wing. Journal of Aircraft. *49*(2), 432-443.

Hamza, M. F., Yap, H. J., & Choudhury, I. A. (2015). Genetic algorithm and particle swarm optimization based cascade interval type 2 fuzzy PD controller for rotary inverted pendulum system. *Mathematical Problems in Engineering 2015*.

Haupt, R. L., & Ellen Haupt, S. (2004). *Practical genetic algorithms.* John Wiley & Sons.

Hernández, C., Naranjani, Y., Sardahi, Y., Liang, W., Schütze, O., & Sun, J.-Q. (2013). Simple cell mapping method for multi-objective optimal feedback control design. *International Journal of Dynamics and Control*, 1(3), 231-238.

Homod, R. Z., Sahari, K. S., Mohamed, H. A., & Nagi, F. (2010). Hybrid PID-cascade control for HVAC system. *International journal of systems control*, *1*(4), 170-175.

Hu, X., Huang, Z., & Wang, Z. (2003). Hybridization of the multi-objective evolutionary algorithms and the gradient-based algorithms. *In The 2003 Congress on Evolutionary Computation, 2003. CEC'03*, Vol. 2, pp. 870-877.

Jones, D. F., Mirrazavi, S. K., & Tamiz, M. (2002). Multi-objective meta-heuristics: An overview of the current state-of-the-art. *European journal of operational research, 137*(1), 1-9.

Kakde, M. R. (2004). Survey on multiobjective evolutionary and real coded genetic algorithms. *In Proceedings of the 8th Asia Pacific symposium on intelligent and evolutionary systems,* (pp. 150-161).

Kaya, I., Tan, N., & Atherton, D. P. (2007). Improved cascade control structure for enhanced performance. *Journal of Process Control*, 17(1), 3-16.

Kumar, C. A., Nair, N., Begum, S., & Tharani, T. (2012a). Multi-objective Cascade Control of Regulatory Process with Two Conflicting Objectives. *Procedia engineering, 38*, 4057-4063.

Kumar, V. S., Laura, A. M., Raymond, K., & Jonathan, E. C. (2012b). Receptance Based Active Aeroelastic Control Using Multiple Control. *53rd AIAA/ASME/ASCE/AHS/ASC Structures, Structural Dynamics, and Materials Conference.* Honolulu, Hawaii: AIAA Paper.

Lee, Y., Park, S., & Lee, M. (1998). PID controller tuning to obtain desired closed loop responses for cascade control systems. *Industrial & engineering chemistry research, 37*(5), 1859-1865.

Liebeck, R. H. (2004). Design of the Blended Wing Body Subsonic Transport. *Journal of Aircraft*, 10-25.

Lucia, D. (2005). The SensorCraft Configurations: A Non-Linear AeroServoElastic Challenge for Aviation. *Proceedings of the 46th AIAA/ASME/ASCE/AHS/ASC Structures, Structural Dynamics and Materials Conference*, (pp. 18-21). Reston, VA.

Maffezzoni, C., Schiavoni, N., & Ferretti, G. (1990). Robust design of cascade control. *IEEE Control Systems Magazine, 10*(1), 21-25.

Marler, R. T., & Arora, J. S. (2004). Survey of multi-objective optimization methods for engineering. *Structural and multidisciplinary optimization, 26*(6), 369-395.

McDonough, L. A., Singh, K. V., & Kolonay, R. (2011). Active Control for Coupled Unsteady Aeroelastic Models. *Proceedings of the International Forum on Aeroelasticity and Structural Dynamics (IFASD 2011).* Paris, France.

Ogata, K., & Yang, Y. (2010). Modern control engineering. *Upper Saddle River, NJ: Pearson*, Vol. 17.

Oral, Ö., Çetin, L., & and Uyar, E. (2010). A Novel Method on Selection of Q And R Matrices In The Theory Of Optimal Control. *International Journal of Systems Control, 1*(2).

Pareto, V. (1971). Manual of political economy.

Sardahi, Y. H. (2016). Multi-objective optimal design of control systems. *Doctoral dissertation, UC Merced*.

Sardahi, Y., & Boker, A. (2018). Multi-objective optimal design of four-parameter PID controls. *In ASME 2018 Dynamic Systems and Control Conference. American Society of Mechanical Engineers Digital Collection*.

Sardahi, Y., & Sun, J.-Q. (2017). Many-objective optimal design of sliding mode controls. *Journal of Dynamic Systems, Measurement, and Control*, 139(1), 014501.

Shibuchi, H., Sakane, Y., Tsukamoto, N., & Nojima, Y. (2009). Evolutionary many-objective optimization by NSGA-II and MOEA/D with large populations. *IEEE International Conference on Systems, Man and Cybernetics*, (pp. 1758-1763).

Singh, K. V., & McDonough, L. A. (2014). Optimization of Control Surface Parameters with Augmented Flutter Boundary Constraints. 20-50.

Singh, K. V., Brown, R. N., & Kolonay, R. (2016). Receptance-based active aeroelastic control with embedded control surfaces having actuator dynamics. *Journal of Aircraft, 0*, 830-845.

Singh, K. V., McDonough, L. A., Kolonay, R., & Cooper, J. E. (2014). Receptance-based active aeroelastic control using multiple control surfaces. *Journal of Aircraft*, 113-136.

Singh, K. V., McDonough, L. A., Mottershead, J., & Cooper, J. (2010). Active Aeroelastic Control Using the Receptance. *Proceedings of the ASME International Mechanical Engineering Congress and Exposition.* Vancouver, BC, Canada.

Smith, C. A., & Corripio, A. B. (1985). *Principles and practice of automatic process control* (Vol. 2). New York: Wiley.

Srinivas, N., & Deb, K. (1994). Muiltiobjective optimization using nondominated sorting in genetic algorithms. *Evolutionary computation, 2*(3), 221-248.

Tian, Y., Cheng, R., Zhang, X., & Jin, Y. (2017). PlatEMO: A MATLAB platform for evolutionary multi-objective optimization [educational forum]. *IEEE Computational Intelligence Magazine, 12*(4), 73-87.

Tunyasrirut, S., & Wangnipparnto, S. (2007). Level control in horizontal tank by fuzzy-pid cascade controller. *World academy of science, engineering and technology, 25*(1).

Wei, X., Jingjing, M., Hongyan, J., & Fei, Y. (2010). The main steam temperature cascade control of high order differential of feedback controller. *In 2010 International Conference on Intelligent System Design and Engineering Application, 2*, 683-687.

Woźniak, P. (2010). Multi-objective control systems design with criteria reduction. *In Asia-Pacific Conference on Simulated Evolution and Learning*, 583-587.

Xu, X., Sardahi, Y., & Zheng, C. (2018). Multi-Objective Optimal Design of Passive Suspension System With Inerter Damper. *In ASME 2018 Dynamic Systems and Control Conference. American Society of Mechanical Engineers Digital Collection*, pp. V003T40A006–V003T40A006.

Zhao, Y. (2009). Flutter suppression of a high aspect-ratio wing with multiple control surfaces. *Journal of Sound and Vibration*, 490-513.

APPENDIX A:

INSITITUTIONAL REVIEW BOARD LETTER

MARSHALL UNIVERSITY.
www.marshall.edu

Office of Research Integrity

February 3, 2020

Yuekun Chen
1739 6th Ave. Apt 33
Huntington, WV 25703

Dear Yuekun:

This letter is in response to the submitted thesis abstract entitled *"Multi-Objective Optimization of Multi-Loop Control Systems."* After assessing the abstract, it has been deemed not to be human subject research and therefore exempt from oversight of the Marshall University Institutional Review Board (IRB). The Code of Federal Regulations (45CFR46) has set forth the criteria utilized in making this determination. Since the information in this study does not involve human subjects as defined in the above referenced instruction, it is not considered human subject research. If there are any changes to the abstract you provided then you would need to resubmit that information to the Office of Research Integrity for review and a determination.

I appreciate your willingness to submit the abstract for determination. Please feel free to contact the Office of Research Integrity if you have any questions regarding future protocols that may require IRB review.

Sincerely,

Bruce F. Day, ThD, CIP
Director

APPENDIX B:

B.1 Aircraft Flexible Wing

The detailed mathematical model of the aircraft wing shown in Figure 14 (see chapter 3) with a leading and trailing control surface is given by

$$\underbrace{\begin{bmatrix} m_T & m_w x_\alpha b \\ m_w x_\alpha b & I_\alpha \end{bmatrix}}_{M}\underbrace{\begin{pmatrix}\ddot{h}\\ \ddot{\alpha}\end{pmatrix}}_{\ddot{q}} + \underbrace{\left(\begin{bmatrix} c_h & 0 \\ 0 & c_\alpha \end{bmatrix} + \rho V b s \begin{bmatrix} C_{l\alpha} & C_{l\alpha}(\frac{1}{2}-a)b \\ -bC_{m\alpha_{\text{eff}}} & -C_{m\alpha_{\text{eff}}}(\frac{1}{2}-a)b^2 \end{bmatrix}\right)}_{C(V)}\underbrace{\begin{pmatrix}\ddot{h}\\ \ddot{\alpha}\end{pmatrix}}_{\ddot{q}}$$
$$+\underbrace{\left(\begin{bmatrix} k_h & 0 \\ 0 & k_\alpha \end{bmatrix} + \rho V^2 b s \begin{bmatrix} 0 & C_{l\alpha} \\ 0 & -bC_{m\alpha_{\text{eff}}} \end{bmatrix}\right)}_{K(V)}\underbrace{\begin{pmatrix}h\\ \alpha\end{pmatrix}}_{q} \tag{B.1}$$
$$= \underbrace{\rho V^2 b \begin{bmatrix} -C_{l\beta_T}(S_{T2}-S_{T1}) & -C_{l\beta_L}(S_{L2}-S_{L1}) \\ bC_{m\beta_{\text{eff}}}(S_{T2}-S_{T1}) & bC_{m\beta_{\text{eff}}}(S_{L2}-S_{L1}) \end{bmatrix}}_{B_{cs}}\underbrace{\begin{pmatrix}\beta_T\\ \beta_L\end{pmatrix}}_{\beta}$$
$$+ \underbrace{\rho V b \begin{bmatrix} -a_w(S_{T2}-S_{T1}) & -a_w(S_{L2}-S_{L1}) \\ bC_{m\beta_{\text{eff}}}(S_{T2}-S_{T1}) & bC_{m\beta_{\text{eff}}}(S_{L2}-S_{L1}) \end{bmatrix}}_{\boldsymbol{B_{ad}}}\underbrace{\begin{pmatrix}w_{g_T}\\ w_{g_L}\end{pmatrix}}_{w_g}$$

The term $\boldsymbol{B_{ad}w_g(t)}$ does not exist in the original model and it was added to show the effect of the aerodynamic loads on the system performance. The elements of $\boldsymbol{B_{ad}}$ were estimated by comparing the values of the control distribution matrix $\boldsymbol{B_{cs}}$ and the aerodynamic load distribution matrix $\boldsymbol{B_{ad}}$ proposed by Kumar et al. (2012b) with those of the model at hand. The 2D lift-curve slope was set to 2π since the ideal lift curve slope of any 2D wing is 2π. In fact, inspecting wind tunnel data for any airfoil shape, it can be found that the slope of the lift curve is very close to this value (Aerospaceweb, 2012). Retrieved from http://www.aerospaceweb.org/question/aerodynamics/q0167.shtml

Symbol	Definition	Value
ρ	air density	1.225,kg/m^3
α	pitching angle (positive nose up)	-0.6719
b	semichord	0.1905,m

r_{cg}	distance from elastic axis to center of mass	-b(0.0998+α) , m
x_a	nondimensional distance from elastic axis to center of mass	r_{cg}/b
s	semispan	0.5945, m
k_h	Plunge stiffness	2844,N/m
k_α	pitch stiffness	12.77,Nm/rad
$C_{l\alpha}$	lift derivative with respect to pitch angle α	6.757
$C_{l\beta_T}$	lift derivative with respect to trailing-edge control angles	3.774
$C_{l\beta_L}$	lift derivative with respect to leading-edge control angles	+1
C_{m_α}		0
c_h	plunge	27.43,kg/s
c_α	pitch damping	$0.036, \text{kg} \cdot m^2/s$
m_w	mass of wing	4.340,kg
m_{wT}	total wing section and mount mass	5.230,kg
m_T	total mass of pitch–plunge system	15.57,kg
I_{cam}	pitch cam moment of inertia	0.04697,kg$\cdot m^2$
I_{cgw}	wing section moment of inertia about the center of gravity	0.04342, kg$\cdot m^2$
I_a	total pitch moment of inertia about elastic axis	$I_{cam} + I_{cgw} + m_w r_{cg}^2$
$C_{m\beta_L}$, $C_{m\beta_{LT}}$	effective trailing- and leading-edge control derivatives, respectively	-0.1005,-0.6719
$C_{m\alpha_{\text{eff}}}$	effective moment derivative	(0.5+α)$C_{l\alpha} + 2C_{m\alpha}$
$C_{m\beta_{\text{Teff}}}$	effective trailing-edge control derivatives	(0.5+α)$C_{l\beta_T} + 2C_{m\beta_T}$
$C_{m\beta_{\text{Leff}}}$	effective leading-edge control derivatives	(0.5+α)$C_{l\beta_L} + 2C_{m\beta_L}$
a_w	2D lift-curve slope	2π

Table 1: The model parameters (Singh et al., 2016)

B.2 Electromagnetic Actuator

The EMA shown in Figure 15 (see Chapter 3) is described by the following equations

$$G_e = \frac{1/R_c}{\frac{L_c}{R_c}s+1} = \frac{1/R_c}{\tau_e s+1}, \tag{B.2}$$

τ_e and $1/R_c$ are the motor's electrical time constant and gain. Assuming that the inductance is very small ($L_c = 0 \rightarrow \tau_e = 0$), which is the case in many inductive loads. The motor's dynamics can be reduced to the following transfer function

G_e=$1/R_c$. (B.3)

The transfer function of the mechanical part of the motor (motor shaft and gearbox) is approximated by G_{mech} such that

$$G_{mech} = \frac{1/K_{mv}}{\frac{J_m}{K_{mv}}s+1} = \frac{K_m}{\tau_m s+1}, \quad \text{(B.4)}$$

Definitions and values of some of the parameters used in the computer simulations are tabulated in Table 2.

Symbol	Definition	Value
J_m	Rotor inertia	0.000391, lb $in.^2$
K_c	Torque constant	2.376, in.lb/A
K_{mv}	Viscous friction and damping	0.00116, in.lb s/rad
K_ω	Back emf constant	0.1342, V s/rad
R_c	Winding resistance	$2.12, \Omega$
τ_m	Mechanical time constant	0.3371, s

Table 2: Motor parameters (Habibi et al., 2008).

B.3 Slider-Crank Mechanism

The kinematic equations of the slider-crank mechanism in Figure 16 (see chapter 3**)** read

$$x = (a + b) - (b\cos\Phi + a\cos\beta)$$

$$X = a\left[\frac{b}{a}(1 - \cos\Phi) + (1 - \beta)\right]$$

Knowing that $\sin\Phi^2 + \cos\Phi^2 = 1$, $\cos\Phi^2 = 1 - \sin\Phi^2$, $\cos\Phi = \sqrt{1 - \sin\Phi^2}$ and setting $n = \frac{b}{a}$, we notice that $\sin\Phi = \frac{\sin\beta}{n}$. After few steps of mathematical substitutions and

simplifications, the relationship between the rock-pinion displacement X and slider-crank angular displacement β can be found as follows

$$\cos\Phi = \sqrt{1-\sin\Phi^2} = \sqrt{1-\frac{\sin\beta^2}{n^2}}$$

$$\mathrm{X} = a\left[n\left(1-\sqrt{1-\frac{\sin\beta^2}{n^2}}\right)+(1-\cos\beta)\right] \qquad \text{(B.5)}$$

$$\frac{X}{a} = \left[n\left(1-\sqrt{1-\frac{\sin\beta^2}{n^2}}\right)+(1-\cos\beta)\right]$$

$$\frac{X}{a} = n - n\sqrt{1-\frac{\sin\beta^2}{n^2}} + 1 - \cos\beta$$

$$\frac{X}{a} = n - n\sqrt{\frac{n^2-\sin\beta^2}{n^2}} + 1 - \cos\beta$$

$$\frac{X}{a} = \mathrm{n} - \sqrt{n^2-\sin\beta^2} + 1 - \cos\beta$$

$$\frac{X}{a} - \mathrm{n} - 1 = -\sqrt{n^2-\sin\beta^2} - \cos\beta$$

$$\sqrt{n^2-\sin\beta^2} + \cos\beta = 1 + n - \frac{X}{a}$$

now, $\sin\beta^2 + \cos\beta^2 = 1 \qquad \sin\beta^2 = 1-\cos\beta^2$

$$\sqrt{n^2-1+\cos\beta^2} + \cos\beta = 1 + n - \frac{X}{a}$$

$$\begin{cases} A = \cos\beta \\ B = 1 + n - \dfrac{X}{a} \end{cases}$$

$$\sqrt{n^2-1+A^2} + \mathrm{A} = B$$

$$n^2 - 1 + A^2 = B^2 + A^2 - 2\mathrm{AB}$$

$$\mathrm{A} = \frac{B^2 - n^2 + 1}{2B}$$

$$\cos\beta = \frac{(1 + n - \frac{X}{a})^2 - n^2 + 1}{2\ (1 + n - \frac{X}{a})}$$

$$\beta = \arccos\frac{(1+n-\frac{X}{a})^2-n^2+1}{2\ (1+n-\frac{X}{a})} \qquad \text{(B.6)}$$